

Review

Recent Progress on Metal Sulfide Composite Nanomaterials for Photocatalytic Hydrogen Production

Sher Ling Lee and Chi-Jung Chang *

Department of Chemical Engineering, Feng Chia University, 100, Wenhwa Road, Seatwen, Taichung 40724, Taiwan; sherlinglee0209@gmail.com

* Correspondence: changcj@fcu.edu.tw

Received: 25 April 2019; Accepted: 13 May 2019; Published: 17 May 2019



Abstract: Metal sulfide-based photocatalysts have gained much attention due to their outstanding photocatalytic properties. This review paper discusses recent developments on metal sulfide-based nanomaterials for H₂ production, acting as either photocatalysts or cocatalysts, especially in the last decade. Recent progress on key experimental parameters, in-situ characterization methods, and the performance of the metal sulfide photocatalysts are systematically discussed, including the forms of heterogeneous composite photocatalysts, immobilized photocatalysts, and magnetically separable photocatalysts. Some methods have been studied to solve the problem of rapid recombination of photoinduced carriers. The electronic density of photocatalysts can be investigated by in-situ C K-edge near edge X-ray absorption fine structure (NEXAFS) spectra to study the mechanism of the photocatalytic process. The effects of crystal properties, nanostructure, cocatalyst, sacrificial agent, electrically conductive materials, doping, calcination, crystal size, and pH on the performance of composite photocatalysts are presented. Moreover, the facet effect and light trapping (or light harvesting) effect, which can improve the photocatalytic activity, are also discussed.

Keywords: metal sulfides; H₂ production; photocatalyst; facet effect; light trapping; crystal size

1. Introduction

Hydrogen, which has high energy yield and less greenhouse gas emissions after combustion, is an environmentally friendly and attractive fuel. Hydrogen production and hydrogen economy, together with potential applications in fuel cell hydrogen electric cars and hydrogen-diesel fuel co-combustion, are hot topics in research related to hydrogen energy [1–8]. Hydrogen is an alternative energy source for fossil fuels. Research on generating electricity from solar energy has also gained increasing attention. Environmentally friendly photocatalytic water-splitting by semiconductor nanomaterials is very important for the development of a hydrogen economy. The photoexcited electron–hole pairs play an important role in the water splitting process. Photocatalysts should be able to absorb radiation and efficiently reduce protons to hydrogen molecules with photogenerated electrons.

Metal sulfide-based photocatalysts are widely investigated because of their unique physical and chemical properties [9–11]. In comparison with their metal oxide analogs, sulfide semiconductors with narrower band gaps hold more promise as photocatalysts for H₂ production [12]. However, the H₂ production performance of metal sulfide-based composite photocatalysts is still limited because of the fast recombination of photoexcited carriers [13]. In addition, photocorrosion is also a major problem for metal sulfide-based photocatalysts. Therefore, many researchers have focused on solving the problems of photocorrosion and carrier recombination, examining the formation of a heterojunction by decorating cocatalysts, introducing noble metal nanoparticles, or using porous conductive substrate.

It has been reported that the formation of a heterojunction interface with other semiconductors or coupling with other cocatalysts can overcome the carrier recombination and photocorrosion problems [14]. The formation of a junction helps to promote the transport of photoexcited electrons. In addition, it is reported that the performance of photocatalysts can also be enhanced further by doping, modifying the surface texture, and tuning the crystal structure [15,16]. Furthermore, current research on metal sulfide-based photocatalysts is focused on two hot topics: the search for novel metal-sulfide nanomaterials that do not contain acutely toxic metals such as cadmium and lead, and the search for cocatalyst nanomaterials that do not contain noble metals.

In this review, we discuss recent developments in the use of metal sulfide-based nanomaterials as either photocatalysts or cocatalysts for H₂ production, especially those in the last 10 years. Recent progress on the fabrication and performance of metal sulfide-based composite photocatalysts is reviewed, including the form of heterogeneous composite photocatalysts, immobilized photocatalysts, and magnetically separable photocatalysts. In addition, the effects of experimental parameters—including noble metal loading, transition metal doping, anion doping, calcination, the pH level of solution, sacrificial agent, structure of photocatalysts, facet effect, light trapping effect, crystal size of photocatalysts, and fabrication methods—on photocatalytic performance are also systematically reviewed.

2. Composite Photocatalysts

2.1. Semiconductor-Based Composite Photocatalysts

2.1.1. Cadmium Sulfide

CdS is a widely-investigated metal sulfide-based photocatalyst that has a narrow band gap and high hydrogen production activity. The synergetic effects of this coupled composite photocatalyst on hydrogen evolution can be studied by investigating the decay behavior of photoexcited carriers. The synergetic effect is important for the enhancement of hydrogen production by sulfides of transition metals. Wang et al. [17] reported that (ZnO)₁/(CdS)_{0.2} composite showed noticeably slower decay kinetics as compared to bare ZnO and CdS when observed with time-resolved fluorescence emission decay spectra. This finding indicates that the photocatalyst (ZnO)₁/(CdS)_{0.2} is able to produce the highest H₂ evolution among different ZnO/CdS heterostructures due to the transfer of photoexcited carriers between CdS and ZnO, which may hinder recombination. A similar trend of this synergetic effect was also observed in other studies, such as those incorporating g-C₃N₄ on the outer shell of a CdS core [18], g-C₃N₄/Ni(OH)₂-CdS [19], g-C₃N₄Ni/CdS [20], co-loading of MoS₂ and graphene to CdS nanorods [21], Ni₃N/CdS [22], and MoS₂/CdS [23]. Transition metal chalcogenides are appropriate candidates for composite photocatalysts due to their conduction band positions, which are appropriate for the reduction reaction of water to form hydrogen [24], and their excellent luminescence and photochemical properties. Table 1 summarizes the photocatalytic performances of CdS-based photocatalysts.

Table 1. Photocatalytic performances of CdS-based photocatalysts.

Photocatalyst	Morphology	Synthetic Method	Sacrificial Agent	Activity ($\mu\text{mol h}^{-1}\text{g}^{-1}$)	Ref. (Year)
CdS/ZnO	Heterostructure	Two-step precipitation	Na_2S , Na_2SO_3	1805	[17] (2009)
g- C_3N_4 /CdS	Core-shell	Solvothermal & chemisorption	Na_2S , Na_2SO_3	4200	[18] (2013)
$\text{Ni}(\text{OH})_2$ -CdS/g- C_3N_4	Core-shell	Mixture	Na_2S , Na_2SO_3	115.2	[19] (2016)
Ni/CdS/g- C_3N_4	Hybrid system	NaBH_4 reduction method	triethanolamine	1258.7	[20] (2016)
MoS_2 -graphene/CdS	Nanoparticle/nanorods	Hydrothermal	Lactic acid	$2320 \mu\text{mol h}^{-1}$	[21] (2014)
Ni_3N /CdS	Nanorods	Two step in-situ growth method	Na_2S , Na_2SO_3	~62	[22] (2016)
MoS_2 /CdS	Heterostructure	Precipitation	Lactic acid	~540	[23] (2008)

2.1.2. Copper Sulfide

CuS/ZnS composites are efficient photocatalysts for hydrogen evolution. Wang et al. reported that CuS/ZnS nanomaterials exhibit high visible light-induced H_2 generation activity. The H_2 generation rate increases with increasing Cu^{2+} ions. However, as with other cocatalysts, when the maximum amount of Cu^{2+} is reached (above 7 mol %), the hydrogen evolution rate decreases significantly. This is due to light shielding by excess CuS, which reduces the number of active sites on the surface [25]. In addition to the solvothermal method for the fabrication of CuS cocatalysts, the growth of CuS/g- C_3N_4 by an in-situ method has been investigated by other authors. That study found that CuS nanoparticles were uniformly distributed on g- C_3N_4 nanosheets [26].

Chang et al. found that CuS-ZnS $_{1-x}$ O $_x$ /g- C_3N_4 heterostructured photocatalyst had a high photocatalytic H_2 generation property. That study demonstrated that the decoration of CuS on the surface helps to enhance the absorption of the heterostructured photocatalyst [27]. In addition, CuS is used to decorate free-standing ZnS-carbon nanotube films because CuS can form heterojunctions with ZnS to improve the separation of photoexcited charge carriers, resulting in higher rates of hydrogen production [28]. In another work, Markovskaya et al. suggested the important role of CuS in enhancing the hydrogen evolution rate of the photocatalyst Cd $_{0.3}$ Zn $_{0.7}$ S. The optimized performance ($3520 \mu\text{mol h}^{-1}\text{g}^{-1}$) was obtained with 1 mol % CuS/Cd $_{0.3}$ Zn $_{0.7}$ S [29]. Similar contributions were also found for CuS/TiO $_2$ nanocomposites [30,31]. Table 2 lists the photocatalytic activity of CuS-based composite photocatalysts.

Table 2. Photocatalytic activity of copper sulfide as the cocatalyst.

Photocatalyst	Structure	Synthetic Method	Sacrificial Agent	Activity ($\mu\text{mol h}^{-1}\text{g}^{-1}$)	Ref. (Year)
CuS/ZnS	Hexagonal plates	Solvothermal	Na_2S , Na_2SO_3	1233.5	[25] (2015)
CuS/g- C_3N_4	Nanocomposites	In-situ growth method	triethanolamine	17.2	[26] (2017)
CuS-ZnS $_{1-x}$ O $_x$ /g- C_3N_4	Heterostructure	Thermal decomposition and hydrothermal	Na_2S , Na_2SO_3 , NaCl	10,900	[27] (2017)
CuS-ZnS/CNTF	Nanocomposite	Hydrothermal	Na_2S , Na_2SO_3 , NaCl	1213.5	[28] (2018)
CuS/Cd $_{0.3}$ Zn $_{0.7}$ S	Nanoparticles	Two-step technique	Na_2S , Na_2SO_3	3520	[29] (2015)
CuS/TiO $_2$	Nanocomposite	Hydrothermal	Na_2S , Na_2SO_3	1262	[30] (2018)
CuS/TiO $_2$	Nanocomposite	Hydrothermal	Methanol	$570 \mu\text{mol h}^{-1}$	[31] (2013)

2.1.3. Silver Sulfide

Recently, silver sulfide was used as a cocatalyst of ZnS photocatalyst to enhance the hydrogen evolution rate. For instance, Hsu et al. reported the use of Ag₂S-coupled ZnO@ZnS core-shell nanorods to achieve efficient H₂ production. The maximum hydrogen production rate is reached when the AgNO₃ concentration is 2 mM; further increasing the concentration only decreases the hydrogen production rate [32]. Figure 1 demonstrates the morphology of and a possible mechanism for the photocatalytic reaction. Because of the growth of Ag₂S on ZnO@ZnS nanorods, photoexcited electrons can effectively transfer from ZnS to Ag₂S or migrate to the conductive wire mesh substrate. The reaction of electrons and H⁺ can produce H₂. Similarly, Yue et al. fabricated a novel Ag₂S/ZnS/carbon nanofiber ternary composite to increase the hydrogen production rate well above that of the reported ZnS composite photocatalyst. In addition, the synergetic effect of Ag₂S and CNF is also important for inhibiting the recombination of charge carriers [33]. Moreover, nanosheets of ZnS:Ag₂S also exhibit a trend of enhancement similar to that of the above mentioned nanostructure. As reported by Yang et al., porous ZnS:Ag₂S nanosheets were synthesized such that the porous nanostructure provided a large surface area for intimate contact with the sacrificial solution [34]. Table 3 shows the H₂ generation performances of photocatalysts loaded with silver sulfide.

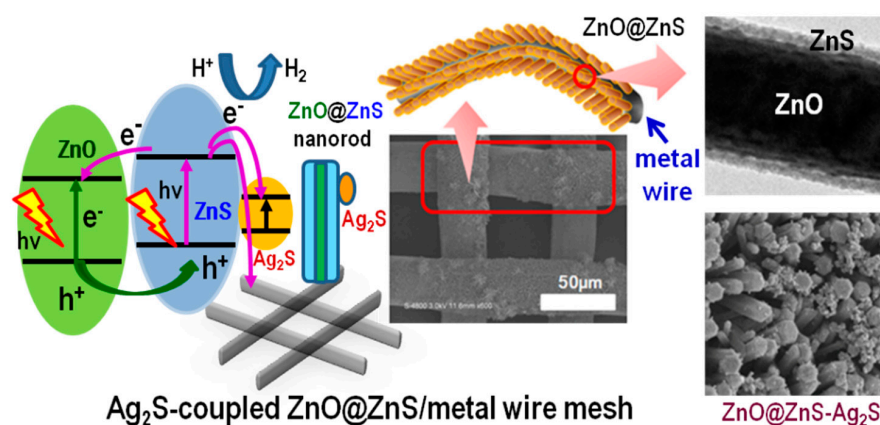


Figure 1. Morphology and a proposed mechanism of the photocatalytic H₂ production by metal wire mesh based immobilized photocatalysts with Ag₂S-coupled ZnO@ZnS core-shell nanorods. Figure adapted from [32].

Table 3. Photocatalytic H₂ generation property of photocatalysts loaded with silver sulfide.

Photocatalyst	Morphology	Synthetic Method	Sacrificial Agent	Activity (μmol h ⁻¹ g ⁻¹)	Ref. (Year)
Ag ₂ S-ZnO@ZnS core-shell	Nanorods	Hydrothermal	Na ₂ S, Na ₂ SO ₃ , NaCl	6406	[32] (2016)
Ag ₂ S/ZnS/carbon nanofiber	Nanofibers	Solid-state process and cation-exchange	Na ₂ S, Na ₂ SO ₃	224.9 μmol h ⁻¹	[33] (2016)
ZnS:Ag ₂ S	Porous nanosheets	Thermal decomposition	Na ₂ S, Na ₂ SO ₃	104.9	[34] (2014)

2.1.4. Zinc Sulfide

ZnS is an excellent photocatalyst for photocatalytic water splitting, for it can produce high negative potentials of photoexcited electrons. Xin et al. reported that ZnS@CdS-Te photocatalysts with a p-n heterostructure exhibited improved H₂ generation rates. Based on the possible mechanism, after the loading of ZnS on the CdS-Te nanostructure, more surface active sites can be produced, leading to increased hydrogen generation activity [35]. Figure 2 presents a possible mechanism of ZnS@CdS-Te

photocatalysts. Moreover, a similar heterojunction between ZnS/g-C₃N₄ has been studied by Hao et al. In that study, the close contact between ZnS and g-C₃N₄ increased the capacity of light harvesting and efficiency of charge separation. The key factor that enhanced the photocatalytic hydrogen was the two-photo excitation of ZnS [36].

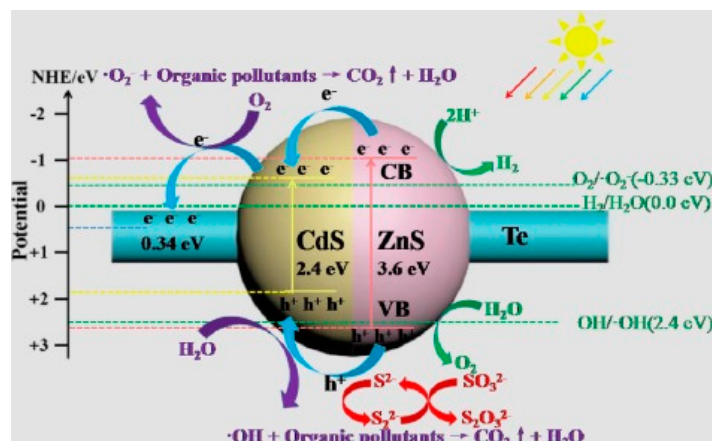


Figure 2. Possible mechanism of ZnS@CdS-Te composite photocatalysts. Figure adapted from reference [35].

In addition to nanostructures, the chloroplast-like structure of Bi₂S₃/ZnS also possesses high photocatalytic activity due to its band gap structure. Based on the reported reaction mechanism, photogenerated electrons migrate from Bi₂S₃ to ZnS to generate H₂, while holes transfer from ZnS to Bi₂S₃. This efficient charge separation improves the H₂ generation rate in this chloroplast-like structure [37].

Efficient H₂ generation has been achieved by CdS-ZnS photocatalyst without facilitation by a cocatalyst. This includes the study done by Jiang et al. on a CdS nanorod/ZnS nanoparticle photocatalyst. The highly efficient hydrogen production likely resulted from the rapid transport of carriers in the core-shell nanorod structure [38]. Table 4 presents the H₂ generation performances of ZnS-based photocatalysts.

Table 4. Photocatalytic H₂ generation performances of ZnS-based photocatalysts.

Photocatalyst	Morphology	Synthetic Method	Sacrificial Agent	Activity (μmol h ⁻¹ g ⁻¹)	Ref. (Year)
ZnS@CdS-Te	p-n heterostructure	Microwave hydrothermal	Na ₂ S-H ₂ O, Na ₂ SO ₃	592.5	[35] (2018)
ZnS/g-C ₃ N ₄	Nanocomposite	One-pot hydrothermal	Na ₂ S, Na ₂ SO ₃	713.68	[36] (2018)
Bi ₂ S ₃ /ZnS	Chloroplast-like structure	Solvothermal	Na ₂ S, Na ₂ SO ₃	176.24	[37] (2017)
CdS/ZnS	Core-shell nanoparticle composite	Solvothermal	Na ₂ S, Na ₂ SO ₃	239 μmol h ⁻¹ mg ⁻¹	[38] (2015)

2.2. Electrically Conductive Materials (Non-Noble Metal)-Based Composite Photocatalysts

2.2.1. Graphene

In addition to decoration with noble and non-noble metals, combining a photocatalyst with graphene or carbon dots is also a useful way to improve activity [39–44]. Graphene can be incorporated solely or co-loaded with other compounds. Loading graphene provides several benefits, such as a large surface area and enhanced separation of photoexcited electron-hole pairs. In other words, the

exceptional electron transfer capability of graphene and intimate contact between the photocatalyst and graphene can help to transport photoexcited electrons efficiently, thus improving the activity for photocatalytic hydrogen generation. As shown in work done by Azarang et al. on nitrogen-doped graphene-supported ZnS nanorods, the photocatalytic activity of ZnS was multiplied by as much as 6 times when solely graphene was loaded and by 14 times when loaded with NG-ZnS [45].

Chang et al. [46] found that the incorporation of graphene with ZnO-ZnS nanoparticles improved the rate of H₂ generation from glycerol. The irradiated and dark states of in-situ C K-edge NEXAFS spectra were monitored to investigate the electronic properties of the photocatalyst. In-situ NEXAFS spectra revealed that photoexcited electrons can be transported from ZnO-ZnS nanomaterials to graphene. NEXAFS spectra were used to investigate the interfacial electronic states of AgI/BiOI/graphene (A10B/G10) samples [47]. Figure 3a–c presents the intensity change (ΔA) between the irradiated and dark states of the Ag L₃-edge, C K-edge, and Bi L₃-edge of BiOI/graphene photocatalyst (BG10), and A10B/G10 photocatalyst. In comparison with BG10, A10B/G10 presents more positive ΔA values of NEXAFS for the Bi L₃-edge and the Ag L₃-edge under in situ light exposure, revealing the increased amounts of the unoccupied density of states (DOS) of the Ag L-edge and Bi L-edge after light exposure due to donating photoexcited electrons for BiOI and AgI. In contrast, compared with A10B/G10, B/G10 exhibits more negative ΔA values of NEXAFS for the C K-edge under light irradiation. The reduced C K-edge indicates the decrease of unoccupied DOS of graphene after light irradiation due to receiving the photoexcited electrons. These results imply the migration of a charge from AgI to BiOI and then to graphene under light exposure. (Figure 3d). The activity can be improved by the formation of graphene/BiOI and BiOI/AgI heterostructures.

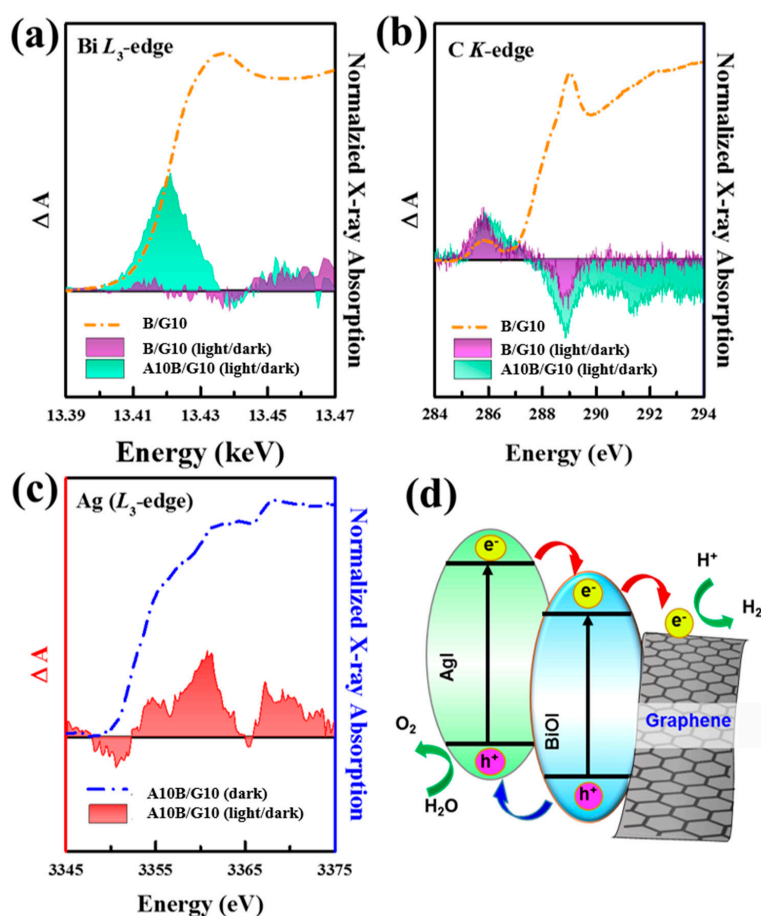


Figure 3. Intensity change between the irradiated and dark states of (a) Bi L₃-edge, (b) C K-edge, and (c) Ag L₃-edge. ($\Delta A = A_{\text{light}} - A_{\text{dark}}$) of B/G10 and A10B/G10 photocatalysts, (d) a proposed mechanism for the photocatalytic H₂ generation reaction by A10B/G10 [47].

The incorporation of graphene provides not only the above-mentioned advantages but also good water dispersity of the composite photocatalyst. This advantage was confirmed by Zhang et al. based on the results of CdSe/CdS-Au (QD-Au) core-satellite heteronanocrystal assembled on graphene nanosheets [48]. In addition to the common graphene nanosheets, Chang et al. also reported using flower-like graphene with a 3D porous structure for application in photocatalytic activity. The application of flower-like graphene enables the photocatalyst to have a higher BET surface area, which leads to enhanced photocatalytic hydrogen production [49]. Table 5 shows the hydrogen generation properties of graphene-loaded composite photocatalysts.

Table 5. Photocatalytic H₂ production properties of graphene-loaded composite photocatalysts.

Photocatalyst	Morphology	Synthetic Method	Sacrificial Agent	Activity (μmol h ⁻¹ g ⁻¹)	Ref. (Year)
MoS ₂ /graphene-CdS	Nanocomposite	Solution-chemistry	Lactic acid	1800 μmol h ⁻¹	[44] (2014)
Nitrogen-doped graphene/ZnS	Nanorods	Thermal annealing of G-ZnS	Na ₂ S, Na ₂ SO ₃ , NaCl	1755.7	[45] (2018)
Graphene/ZnO-ZnS	Particle-on-sheet	Two-step heating	Glycerol	1070	[46] (2018)
Graphene/CdS	Nanocomposite	Solvothermal	Lactic acid	1120 μmol h ⁻¹	[47] (2011)
CdSe/CdS-Au-graphene	Nanocrystals	SILAR technique	Na ₂ S, Na ₂ SO ₃	3113	[48] (2014)
Graphene/ZnS	Nanocomposite	Hydrothermal	Na ₂ S, Na ₂ SO ₃ , NaCl	11,600	[49] (2017)

2.2.2. Reduced Graphene Oxide and Graphene Oxide

Since the discovery of graphene (G) and/or graphene oxide (GO) [50], they have been widely studied [51–53]. GO consists of graphene nanosheets with epoxy or hydroxyl group-modified basal planes and carbonyl/carboxylic acid-modified edges [54–56]. In contrast to graphite, GO can be exfoliated easily and dispersed in aqueous solution because of these hydrophilic groups on the surface [57–59]. Hence, a few studies have used graphene oxide as the supporting material. For instance, in a recent study done by Peng et al., GO-cadmium sulfide was immobilized and well dispersed on a graphene oxide sheet. Increasing the GO-loading up to 5 wt % promoted the hydrogen generation rate to a maximum of 314 μmol h⁻¹ [60]. Hou et al. found that the introduction of GO can extend the lifetime of the photoexcited carriers because they can act as both electron transporter and electron acceptor [61].

A number of authors have also driven the further development of reduced graphene oxide. For instance, Zhang et al. enhanced solar photocatalytic hydrogen production by introducing reduced graphene oxide nanosheets and Zn_xCd_{1-x}S. That research provided a green method for using reduced graphene oxide (RGO) as a support material to enhance the performance of Zn_xCd_{1-x}S photocatalyst, for the hydrogen production of RGO-Zn_{0.8}Cd_{0.2}S was 450% higher than that of pristine Zn_{0.8}Cd_{0.2}S [62]. Similar effects after the incorporation of reduced graphene oxide have been evidenced in other works, such as studies of ZnO-CdS/RGO [63] and ternary NiS/Zn_xCd_{1-x}S/RGO nanocomposites [64]. Table 6 presents the photocatalytic H₂ production properties of graphene oxide loaded with composite photocatalysts.

Table 6. Photocatalytic H₂ production for graphene oxide loaded with composite photocatalysts.

Photocatalyst	Morphology	Synthetic Method	Sacrificial Agent	Activity ($\mu\text{mol h}^{-1}\text{g}^{-1}$)	Ref. (Year)
GO-CdS	Nanocomposite	Precipitation	Na ₂ S, Na ₂ SO ₃	314 $\mu\text{mol h}^{-1}$	[60] (2012)
GO-CdS@TaON	Hybrid composites	Hydrothermal	Na ₂ S, Na ₂ SO ₃	633 $\mu\text{mol h}^{-1}$	[61] (2012)
RGO-Zn _x Cd _{1-x} S	Nanocomposite	Coprecipitation-hydrothermal	Na ₂ S, Na ₂ SO ₃	1824	[62] (2012)
ZnO-CdS/RGO	Heterostructure	Light irradiation-induced reduction	Na ₂ S, Na ₂ SO ₃	510 $\mu\text{mol h}^{-1}$	[63] (2014)
NiS/Zn _x Cd _{1-x} S/RGO	Ternary nanocomposite	Coprecipitation-hydrothermal	Na ₂ , Na ₂ SO ₃	205.9 $\mu\text{mol h}^{-1}$	[64] (2014)

2.2.3. Conductive Polymer

Many papers have reported on the improvement of photocatalytic activity due to the loading of conductive polymers, such as polythiophene, polypyrrole, PEDOT, and PSS. Conductive polymers are capable of inducing charge separation in the composite photocatalysts [65]. A recent study showed that polyaniline (PANI)/ZnS synthesized by solvothermal method increases the hydrogen evolution rate up to $6750 \mu\text{mol h}^{-1}\text{g}^{-1}$ because PANI has unique electron and hole transporting properties [66]. PANI-ZnS composite photocatalysts exhibit improved dispersibility, light harvesting, and photocurrent response. Wang et al. [67] also reported on conducting polymers (such as polypyrrole, poly-3,4-ethylenedioxythiophene (PEDOT), and PANI) on the surface of CdS nanorods. It was found that the rate of hydrogen production of polyaniline@CdS was almost 5 times that of PEDOT@CdS and 3 times that of polypyrrole@CdS. That study showed that polyaniline is an efficient conducting material for modifying CdS nanomaterials, for it enables better light penetration than does a polypyrrole shell. Zielińska et al. [68] reported that the hydrogen production of PANI/NaTaO₃ photocatalyst under UV light irradiation was about twice that of pristine NaTaO₃ photocatalyst. PANI/NaTaO₃ exhibits a lower PL spectrum than that of NaTaO₃, indicating a slower recombination of photoexcited charge carriers. The photoluminescence (PL) spectrum confirmed that the enhancement resulted from the efficient charge separation process. Sasikala et al. studied the photocatalytic hydrogen production performance of MoS₂-PANI-CdS photocatalysts [69]. The incorporation of MoS₂ and PANI improved the visible light absorption ability and improved the lifetime of photoexcited electron-hole pairs of the composite photocatalysts. To achieve high photocatalytic activity, 4% MoS₂ and 5% PANI are the optimum amounts for the composite photocatalysts. The enhanced light absorption and lifetime of the photoexcited charge carriers result in improved activity of the photocatalysts. Figure 4 presents a possible mechanism for the electron transfer of MoS₂-PANI-CdS photocatalysts. Incorporating polyaniline helps to separate photoinduced charges across the ZnS-polyaniline interfaces.

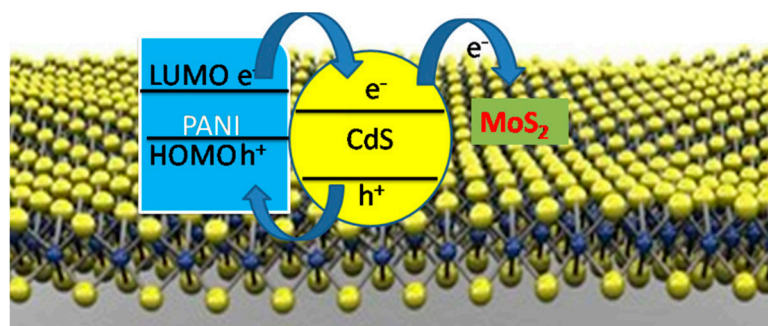


Figure 4. A proposed mechanism for the electron transfer of MoS₂-PANI-CdS photocatalysts when illuminated. Figure adapted from [69].

2.2.4. Conductive Substrate

Chang et al. studied the performance of Ni-doped ZnS/NiO/Ni foam photocatalysts [70]. Ni foam was decorated with doped ZnS to prepare the porous immobilized photocatalysts. The photocatalysts had an optimized activity of $2500 \mu\text{mol/g}^{-1} \text{h}^{-1}$, resulting from their matched band structure, porous microstructure, and conductive Ni foam as substrate. The surface turned from hydrophobic to superhydrophilic after Ni-doped ZnS was grown on the surface of the Ni foam. In addition, the porous microstructure facilitated the transport of reactant and generated a large amount of surface active sites, and the conductive Ni foam aided in the separation of photoexcited carriers. Figure 5 shows a proposed mechanism, illustrating the band structure of the photocatalysts and the transport of photoexcited electrons. When the composite photocatalysts were irradiated with light, the photoexcited electrons were effectively separated by their transportation from ZnS to NiO. In addition, stainless-steel wire mesh is also a good candidate for the preparation of porous immobilized photocatalysts [71].

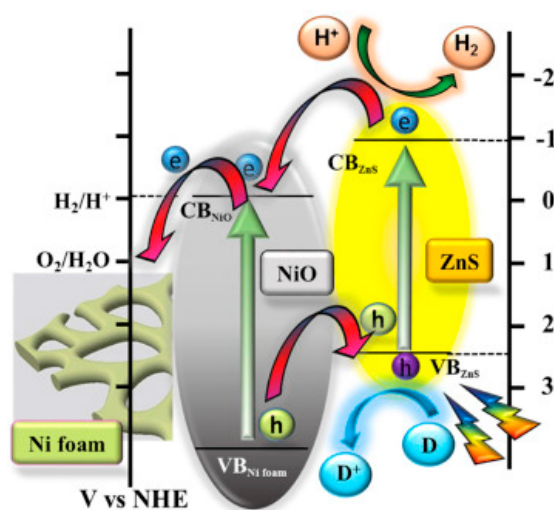


Figure 5. A possible mechanism for the photoexcitation and carrier transporting process of Ni-doped ZnS/NiO/Ni foam photocatalysts. Figure adapted from [70].

2.3. Magnetic Materials-Based Composite Photocatalysts

Magnetic nanomaterials have been used as the core for the preparation of magnetically separable photocatalysts. To improve the activity, photocatalyst nanomaterials should be highly dispersible in solution. Nonetheless, it will become more difficult to separate and reuse the nanoparticles of photocatalysts by centrifugation for repeated operation if such good dispersal stability is achieved. Hence, the introduction of magnetic nanomaterials in photocatalysts will enable efficient separation for the repeated use of photocatalysts. For instance, in studies conducted on $\text{NiCo}_2\text{O}_4@\text{ZnS}$ and $\text{Fe}_3\text{O}_4@\text{ZnS}$ core-shell nanoparticles, the recycled photocatalyst exhibited a good hydrogen evolution rate even after being recycled three times [72]. The ZnS shell deposited on a magnetic core decreases the magnetic saturation of core-shell microspheres. $\text{CoFe}_2\text{O}_4@\text{ZnS}$ nanoparticles exhibit superparamagnetic properties where no residual magnetism is left after repeated use of the photocatalyst [73]. Figure 6 shows the dispersion and magnetic separation of calcinated $\text{CoFe}_2\text{O}_4@\text{ZnS}$ -0.5h photocatalyst. The superparamagnetic property is quite important for photocatalytic H_2 generation in practical operations. After the magnet is removed, there should be no residual magnetism so as to prevent the aggregation of recycled photocatalysts.

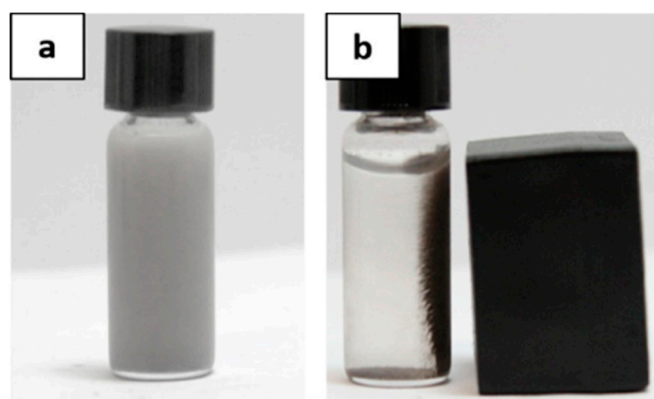


Figure 6. (a) Dispersion of $\text{CoFe}_2\text{O}_4@\text{ZnS}$ -0.5h photocatalysts, (b) the separation of $\text{CoFe}_2\text{O}_4@\text{ZnS}$ -0.5h photocatalyst by an external magnet. Figure adapted from [73].

3. Experimental Parameters for Enhancing Photocatalytic Activity

3.1. Loading with Metal

The majority of the prior research to improve the activity of photocatalysts involved the loading of noble and non-noble metals and the coupling of semiconductors. Then the photogenerated electrons could be transported to the noble metals or delocalized and transported between photocatalysts.

3.1.1. Noble Metal Loading

The photocatalytic activity for the production of hydrogen is affected by the noble metal loaded on the photocatalyst. Noble metal co-catalysts can accelerate the transport of photoexcited charge and thus create H_2 desorption sites. This will eventually lead to higher H_2 generation activity [74]. Although the rate of H_2 generation will increase with increasing noble metal loads, the loading amount will reach a maximum, above which further increases of a noble metal will not decrease the photocatalytic activity. The reduction is probably due to two factors: (i) excess noble metal will lead to shielding of the incident light; and (ii) a higher amount of noble metal decorated on the photocatalyst surface will cause light scattering of the samples, thus reducing the effective irradiation absorbed by the reaction suspension [75,76].

Zhou et al. studied the ternary heterojunction photocatalyst $\text{CdS}/\text{M}/\text{TiO}_2$ ($\text{M} = \text{Ag}, \text{Au}, \text{Pd}, \text{Pt}$). Some photocatalysts enriched with the noble metals are better than pristine TiO_2 and binary heterojunction photocatalysts. For example, the hydrogen evolution rate of photocatalyst loaded with Pd ($\text{CdS}/\text{Pd}/\text{TiO}_2$) is 6.7 times higher than that of CdS/TiO_2 [77].

The photocatalytic H_2 generation activity also increases as greater amounts of Au are loaded onto ZnS flowers. When the Au load is less than 4%, the photocatalytic activity is able to reach $3306 \mu\text{mol h}^{-1}\text{g}^{-1}$. Further increasing the Au load to 6% reduces the activity. Such improvement of photoactivity can be ascribed to the following reasons. First, in comparison with the conduction band minimum of ZnS, Au has a lower Fermi level. The photoexcited electrons can be transported to Au. Second, the Au(I) loaded on the ZnS lattice will extend the light absorption wavelength and enhance the light harvesting efficiency [78]. Moreover, when Au nanoparticles are incorporated on S,N-modified TiO_2 (SNT), the Au particles promote the visible light-driven hydrogen production activity. Because of surface plasmon resonance, 3.5 nm Au particles deposited on TiO_2 can increase light absorption. The amount of hydrogen generated by the 3Au-SNT is 9 times that of pure SNT [79].

In addition to Au, Pt is frequently incorporated in semiconductor photocatalysts. In a previous study by Yu et al., Pt was loaded onto a $\text{Cu}_2\text{ZnSnS}_4$ (CZTS) semiconductor with a maximum content of 1%, and the hydrogen production rate increased. However, the performance decreased when the Pt load was further increased, due to the optical shielding effect. The production of hydrogen by 1% $\text{Cu}_2\text{ZnSnS}_4$ -Pt was 8 times higher than that of bare $\text{Cu}_2\text{ZnSnS}_4$. Intimate contact between CZTS and Pt

increases the production of hydrogen [80]. Similarly, in CdS photocatalyst, the hydrogen evolution reaches a quantum efficiency of 51% and a maximum of $4800 \mu\text{mol h}^{-1}$ when 0.65 wt % of Pt is loaded on CdS. However, the activity can be further increased by loadings of 0.3 wt % Pt and 0.13 wt % PdS on CdS. The co-loading of noble and non-noble metals onto pristine CdS promotes the splitting of H_2S into H_2 and S [81]. Likewise, the addition of Pt to CuS-TiO_2 enhances the evolution of hydrogen because excited electrons from the CB of CuS or through CB of TiO_2 can be transferred directly to Pt sites, resulting in the reduction of protons to hydrogen [82]. Moreover, loading Pt on novel $\text{Cd}_x\text{Cu}_y\text{Zn}_{1-x-y}\text{S}$ also enhances the photocatalytic performance. The presence of 0.5 wt % Pt increases the H_2 production rate to $557 \mu\text{mol h}^{-1}$, as compared to $350 \mu\text{mol h}^{-1}$ produced by $\text{Cd}_{0.1}\text{Cu}_{0.01}\text{Zn}_{0.89}\text{S}$ alone [83].

The presence of Cu in a photocatalyst facilitates carrier separation and also increases light absorption. As reported in a study of In and Cu co-doped ZnS photocatalysts by Kimi et al. [84], photocatalytic performance is strongly related to the amount of doped Cu. With the suitable amount of doped Cu (0.03), hydrogen evolution reaches a maximum that is 8 times higher than that of hydrogen produced by In(0.1)-ZnS photocatalyst. However, with the incorporation of more Cu, the photocatalytic activity becomes lower than that of single doped In(0.1)-ZnS. An excessive amount of Cu causes light scattering, and the excess Cu also acts as recombination sites to halt the photocatalytic reaction.

Although the incorporation of noble metals in photocatalysts will increase the rate of hydrogen production, different noble metals have various effects on the enhancement. When four different noble metals, Pt, Rh, Pd, and Ru, are decorated on CdS/TiO_2 photocatalyst, the amount of photogenerated H_2 by Pt loaded ($640 \mu\text{mol h}^{-1}$) photocatalyst is the highest [85]. Table 7 shows the photocatalytic H_2 generation for noble metal-loaded photocatalysts.

Table 7. Photocatalytic H_2 generation for noble metal-loaded photocatalyst.

Photocatalyst	Noble Metal	Synthetic Method	Activity ($\mu\text{mol h}^{-1} \text{g}^{-1}$)	Ref. (Year)
CdS/M/TiO_2	Au, Ag, Pt	Two-step photodeposition	-	[77] (2014)
ZnS flower	Au	Deposition-precipitation	3306	[78] (2013)
S,N-TiO ₂	Au	Deposition-precipitation	267.6	[79] (2014)
$\text{Cu}_2\text{ZnSnS}_4$	Pt	-	1020	[80] (2014)
CdS	Pt	Photodeposition	$8770 \mu\text{mol h}^{-1}$	[81] (2009)
CuS-TiO_2	Pt	Hydrothermal	746	[82] (2016)
$\text{Cd}_x\text{Cu}_y\text{Zn}_{1-x-y}\text{S}$	Pt	Co-precipitation	$557 \mu\text{mol h}^{-1}$	[83] (2008)
In(0.1),Cu(x)-ZnS	Cu	Hydrothermal	$16.6 \mu\text{mol h}^{-1}$	[84] (2016)
CdS/TiO_2	Pt	Precipitation	Pt: $640 \mu\text{mol h}^{-1}$	[85] (2007)
ZnO-CdS	Pt	Modified hydrothermal	6180	[86] (2010)

3.1.2. Transition Metal Doping

As observed from a few recent studies, transition metals (TM) have begun attracting attention because doping with TM can significantly enhance the photocatalytic performance by efficiently promoting the separation process of photoexcited holes and electrons. For instance, Chen et al. developed an in-situ photodeposition method to load Co on CdS nanorods. That work reported a highest photocatalytic activity of $1299 \mu\text{mol h}^{-1}$ with the optimum loading of 1.0 wt % [87]. In comparison with nickel and iron, cobalt has the ability to improve the rate of H_2 generation. From the work done by Zhou et al., the enhancement of the activity of MoS_x was found to be in the order of $\text{Co} > \text{Ni} > \text{Fe}$ [88]. This improved performance results from the higher amount of doped Co and the capability of Co to activate the S-edge sites [89]. A quick screening technology has been reported to find out the optimized composition of the photocatalyst. M-ZnS based photocatalysts (M = Cr, Cu, Ni, Mo, and Ag) for photoelectrochemical water oxidation applications can be screened rapidly using scanning electrochemical microscopy (SECM) with an optical fiber by finding, the spot with the highest photocurrent among the photocatalyst arrays [90].

Ni doping can enhance the photocatalytic activity of H₂ generation by increasing the absorption of light of the doped photocatalyst. In contrast, when the amount of Ni loaded on ZnS-graphene composites is increased, it will degenerate the crystalline property of the photocatalyst [91]. In addition, the incorporation of Ni on Cd_{1-x}Zn_xS microsphere photocatalyst increases the rate of hydrogen production to 191 μmol h⁻¹g⁻¹ when an optimum amount of 0.1 wt % Ni is loaded. The increment results from the decreased particle size and increased surface area of the photocatalyst [92]. Incorporating a metal such as Ni onto the photocatalyst can accelerate the process of transferring electrons to the surface and decrease the band gap, leading to increased photocatalytic activity. A similar trend of enhancement by Ni doping was also observed with stainless steel wire mesh@doped ZnS photocatalyst [93]. Pristine stainless steel wire mesh C60 has a hydrophobic surface (water contact angle = 103°). In contrast, the water contact angle of ZnS decorated wire mesh photocatalyst C60S0.5 is 0°. Effective contact between the sacrificial solution and the photocatalyst surface is very important because the photocatalyst is used for photocatalytic H₂ generation in aqueous sacrificial solution. Improving the hydrophilicity of the photocatalyst will lead to increased activity. Table 8 lists the photocatalytic H₂ production performances for transition metal doped photocatalysts.

Table 8. Photocatalytic hydrogen production performances for transition metal doped photocatalysts.

Photocatalyst	Dopant	Synthetic Method	Sacrificial Agent	Activity (μmol h ⁻¹ g ⁻¹)	Ref. (Year)
CdS	Co	In-situ photodeposition	(NH ₄) ₂ SO ₃	1299 μmol h ⁻¹	[87] (2018)
MoSG	Co	Solvothermal	TEOA-H ₂ O	11,450	[88] (2019)
ZnS-graphene	Ni	chemical vapor deposition	Na ₂ S, Na ₂ SO ₃ , NaCl	8683	[89] (2015)
Cd _{1-x} Zn _x S	Ni	Hydrothermal	Na ₂ S, Na ₂ SO ₃	191	[92] (2008)
Stainless steel@ZnS	Ni	Solvothermal	Na ₂ S, Na ₂ SO ₃ , NaCl	14,600	[93] (2014)

3.2. Non-Metal Doping

Gopinath et al. [94] reported that the band gap of semiconductor oxide was reduced by doping with anions because of the broadening or the upward shifting of VB. Asahi et al. [95] studied the effects of C, N, F, P, or S doping on TiO₂-based photocatalysts. Their results showed that N doping can decrease the band gap of the photocatalyst due to the energy state overlapping between the N 2p states and O 2p states. Such band gap narrowing was also found for S doped photocatalysts. Up to the present, only a few studies have demonstrated the use of anion doping to improve the visible light-induced hydrogen generation performance. As non-metal doping is more difficult to prepare by conventional chemical methods, it has received little attention. Tsuji et al. demonstrated the effectiveness of halogen codoped Pb-ZnS photocatalyst in photocatalytic activity. Although Pb-doped ZnS already has a high hydrogen evolution rate, codoping of halogen is still useful, for it facilitates the relaxation of the distortion produced by doping with large Pb ions. The photocatalytic activity of halogen and Pb codoped ZnS is three times higher than that of the Pb-doped ZnS photocatalyst [96].

3.3. Calcination

By changing the treatment temperature and ambient gas condition, the post thermal treatment of metal sulfide photocatalysts at elevated temperature in air or oxygen usually results in effective electron-hole separation and enhanced photocatalytic activity, due to the formation of metal sulfide-metal oxide heterojunction. Hong et al. [97] reported that ZnS-ZnO composite prepared by thermal treatments from preformed ZnS particles showed improved charge separation and photocatalytic

activity. Optimizing oxide content in ZnS–ZnO photocatalyst by controlling O₂ partial pressure (16.9 kPa) and temperature (500 °C) can help to achieve a H₂ production rate of 494.8 μmol g⁻¹ h⁻¹.

The crystallinity and surface area of a photocatalyst can be modified by calcination. Based on previous studies, the H₂ production rate increases as the calcination temperature increases. However, there is an optimum temperature for the maximum H₂ evolution rate. Further increment of temperature will cause negative effects on the H₂ production rate. This negative effect results from the decrease in the surface area after heating at high temperature. These findings have been evidenced in Ce-doped ZnO/ZnS [98], ZnS_{1-x-0.5y}O_x(OH)_y(1:1)T₁-673 [99], and CdS/TiO₂ [85]. Table 9 presents the influence of calcination treatment on the activity of photocatalysts.

Table 9. Effects of calcination treatment on photocatalytic performance.

Photocatalyst	Synthesis Method	Optimum Temperature (K)	Surface Area (m ² /g)	Activity (μmol h ⁻¹ g ⁻¹)	Ref. (Year)
Ce-doped ZnO/ZnS	precipitation	673	51.25	1200	[98] (2015)
ZnS _{1-x-0.5y} O _x (OH) _y (1:1)T ₁ -673	Co-precipitation	373	72.4	~375 μmol	[99] (2009)
CdS/TiO ₂	Precipitation and sol-gel method	773	~25	~620 μmol h ⁻¹	[85] (2007)

3.4. Effects of pH Level

The photocatalytic evolution of hydrogen is affected by the pH level of the sacrificial agent solution. However, the effect of pH on photocatalytic performance depends on the mechanism of the reaction. According to previous research by Markovskaya et al., the pH level of the sacrificial agent can be manipulated by adding NaOH or acetic acid. The addition of acetic acid initially increases the rate of hydrogen evolution, up to a sharp peak at pH 7.5. Further increasing the acetic acid causes a drop in the evolution rate. The H₂ production in Na₂S/Na₂SO₃ is described as [29]



According to reaction (1) of the reaction mechanism, the addition of hydroxyl ions thermodynamically impedes the H₂ production reaction, while an increase in the concentration of acetic acid promotes the reaction. The dependence of the H₂ generation rate on the pH level has been reported for Ni-doped CdS nanorods [100]. Both samples under pH 14.7 conditions performed better than the other two. These results suggested that the concentration of OH⁻ is an important factor that will affect the efficiency of hydrogen generation.

3.5. Sacrificial Agent

The sacrificial agent plays the important role of electron donor, efficiently consuming holes to prevent recombination of charge carriers on the surface of the photocatalyst [100]. Charge recombination is one of the factors that may hinder the performance of photocatalytic reactions. Adding suitable sacrificial agents helps to solve the problem. For different reactions, different sacrificial agents should be used. For photocatalytic hydrogen production reactions, the sacrificial agent acts as the hole scavenger to reduce the charge recombination of the photoexcited electron–hole pairs. Then electrons can react with H⁺ and enhance the photocatalytic performance for hydrogen production. Metal sulfide-based photocatalysts exhibit excellent activities in aqueous solution containing sacrificial reagents Na₂S and Na₂SO₃. In addition to Na₂S and Na₂SO₃, some other candidates—such as methanol [31], triethanolamine [20,101], lactic acid [23,44], glycerol [46], and 2-propanol [102]—can act as the sacrificial agents for metal oxysulfide or metal oxide/metal sulfide composite photocatalysts. It will be more constructive from the viewpoints of energy production and environmental protection if the sacrificial agents are sourced from the chemical waste or byproducts of industrial processes. One example is glycerol, which is a byproduct of biodiesel manufacturing. In the chemical industry, sulfur-containing side products and waste are common. In addition to the type of sacrificial agent, its

concentration also affects the photocatalytic activity. As an example, the effect of glycerol concentration on the performance of photocatalysts has been studied [46]. Glycerol can react with photogenerated holes to hinder the recombination of electron–hole pairs. Optimized graphene and glycerol contents can achieve the maximum H₂ generation activity (1070 $\mu\text{mol h}^{-1}\text{g}^{-1}$). Table 10 lists the photocatalytic activity of photocatalysts using different sacrificial agents.

Table 10. Photocatalytic activity of photocatalysts using different sacrificial agents.

Photocatalyst	Morphology	Synthetic Method	Sacrificial Agent	Activity ($\mu\text{mol h}^{-1}\text{g}^{-1}$)	Ref. (Year)
Ni/CdS/g-C ₃ N ₄	Hybrid system	NaBH ₄ reduction method	Triethanolamine	1258.7	[20] (2016)
MoS ₂ /CdS	Heterostructure	Precipitation	Lactic acid	~540	[23] (2008)
CuS/TiO ₂	Nanocomposite	Hydrothermal	Methanol	570 $\mu\text{mol h}^{-1}$	[31] (2013)
MoS ₂ /graphene-CdS	Nanocomposite	Solution-chemistry	Lactic acid	1800 $\mu\text{mol h}^{-1}$	[44] (2014)
Graphene/ZnO-ZnS	Particle-on-sheet	Two-step heating	Glycerol	1070	[46] (2018)
ZnIn ₂ S ₄ /g-C ₃ N ₄	Heterojunction nanosheets	In-situ growth	Triethanolamine	5.2 $\mu\text{mol h}^{-1}$	[101] (2016)
CdS/CdSe	Nanorods	-	2-propanol	40 mmol/h-g	[102] (2010)

3.6. Morphology

The morphology of a photocatalyst also affects the performance, for the surface area and the surface active sites are influenced by the structure. Photocatalysts have different morphologies, including 3D and porous morphologies, nanosheets, nanorods, nanoflowers, and nanowires [14,19,25,32,34,47,77,103]. Recently, Amirav et al. studied tunable nanorod heterostructures. They demonstrated that a longer CdSe seeded rod was more active than a shorter rod of the same diameter, as the surface active sites were located further apart. However, nanorods with comparable rod lengths but smaller diameters will provide higher activity [102]. Panmand et al. reported that more structural defects and surface states are created on CdS decorated Bi₂S₃ nanowires. Figure 7 presents the morphology of a composite photocatalyst. The photogenerated charge carriers of photocatalysts with such defect energy levels can be effectively separated, leading to enhanced photocatalytic activity [104].

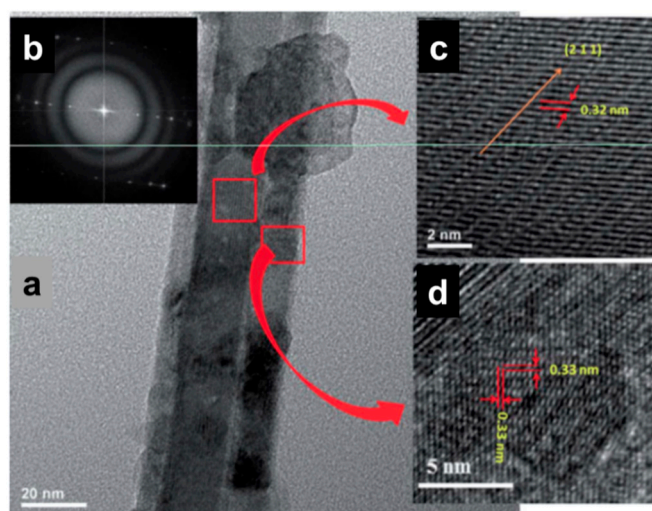


Figure 7. (a) HRTEM image; (b) SAED pattern of CdS decorated Bi₂S₃ nanowires; magnified HRTEM images of (c) Bi₂S₃ nanowire; (d) CdS nanoparticle [104].

In addition, a 2D morphology (such as a nanosheet) can help to improve the photocatalytic activity. Zhang et al. reported that ZnIn₂S₄/g-C₃N₄ heterojunction nanosheets demonstrated higher H₂

production rates compared to single heterojunction components [101]. The contact of the components to form heterojunctions is very important [105]. A nanorod array structure with a small inter-rod distance will not easily form heterojunctions with close contact between different components. In contrast, a 2D heterostructure has enhanced photocatalytic performance because the van der Waals interaction of the 2D heterostructure junction between 2D metals (1T-MoS₂) and the 2D semiconductor (O-g-C₃N₄) minimizes the Schottky barrier, thus improving the efficiency of charge transfer [106].

Moreover, the notable high hydrogen production rate and good stability achieved by mesoporous monoclinic CaIn₂S₄ with surface nanostructures implies the importance of structure in enhancing the H₂ evolution rate. Ding et al. reported that monoclinic CaIn₂S₄ (m-CaIn₂S₄) exhibits a lower ability than cubic CaIn₂S₄ (c-CaIn₂S₄) to absorb visible light, but it also has better photocatalytic performance. The better performance results from the larger surface area, higher pore volume, more negative conduction band potential, and efficient separation of photoexcited carriers of m-CaIn₂S₄ [107].

Furthermore, a core-shell structure will also benefit the photocatalyst, as it may have an increased surface area and change the surface properties. For example, Chang et al. reported that the growth of Ag₂S-ZnO@ZnS core-shell nanorods on metal wire mesh had modified the surface from hydrophobic to superhydrophilic. In addition, the H₂ production activity also increased with the increasing thickness of the ZnS shell [32]. A similar trend was also evidenced in studies of NiCo₂O₄@ZnS and Fe₃O₄@ZnS core shell photocatalysts [72]. Table 11 presents the performances of photocatalysts with different structures.

Table 11. Photocatalytic activity of photocatalysts with different structures.

Photocatalyst	Morphology	Synthetic Method	Sacrificial Agent	Activity (μmol h ⁻¹ g ⁻¹)	Ref. (Year)
ZnIn ₂ S ₄ /g-C ₃ N ₄	Heterojunction nanosheets	In-situ growth	Triethanolamine	5.2 μmol h ⁻¹	[104] (2016)
CdS/CdSe	Nanorods	-	2-propanol	40 mmol h ⁻¹ g ⁻¹	[102] (2010)
CdS/Bi ₂ S ₃	Nanowires	In-situ growth	H ₂ S, KOH	4560	[103] (2016)
CaIn ₂ S ₄	Mesoporous monoclinic with surface nanostructure	High temperature sulfurization	Na ₂ S, Na ₂ SO ₃	3.02 mmol h ⁻¹ g ⁻¹	[106] (2018)
CaIn ₂ S ₄ /g-C ₃ N ₄	Heterojunction nanocomposite	Two-step method	Na ₂ S, Na ₂ SO ₃	102	[107] (2014)
ZnIn ₂ S ₄	3D hierarchical persimmon-like shape	Oleylamine (OA)-assisted solvothermal	Na ₂ S, Na ₂ SO ₃	220.45 μmol h ⁻¹	[108] (2012)
Ag ₂ S-coupled ZnO@ZnS	Core-shell	Sulfidation	Na ₂ S, Na ₂ SO ₃ , NaCl	5310	[32] (2016)
NiCo ₂ O ₄ @ZnS	Core-shell	Solvothermal	Na ₂ S, Na ₂ SO ₃ , NaCl	3900	[72] (2015)
Fe ₃ O ₄ @ZnS	Core-shell	Solvothermal	Na ₂ S, Na ₂ SO ₃ , NaCl	880	[72] (2015)

3.6.1. Facet Effect

It has been reported that the photocatalysis reaction mainly occurs at the surface of the photocatalyst. The exposure of certain facets leads to greatly improved activity of the photocatalysts, known as the facet effect. Therefore, the preparation of photocatalysts with specific morphologies and structures is an important topic in the photocatalysis field. The facet effect has been observed for some oxide-based photocatalysts. Li et al. [109] reported that efficient separation of photoexcited electron-hole pairs can occur between different facets of photocatalytic nanomaterials. In comparison with their analogs with randomly distributed cocatalysts, selective deposition of a reduction cocatalyst and an oxidation cocatalyst on the {010} and {110} facets of BiVO₄ leads to higher photocatalytic activity. Ohno et al. [110] found the effect of facets on the photocatalytic activity of TiO₂ photocatalysts. For the rutile TiO₂ nanomaterials, the {110} facet can act as an effective reduction site, and the {011} facet can offer a site for effective oxidation. TiO₂ photocatalysts show high activity because of the synergistic effect between the {110} and {011} facets.

Similar results were also found for the sulfide-based photocatalysts. Song et al. found that, in comparison with 2-D Cu_2MoS_4 nanosheet with the exposed {001} facet, Cu_2MoS_4 nanotube with the exposed {010} facet exhibited effectively improved the performance for photocatalytic degradation and water splitting [111]. Shen et al. reported that the crystal facets of ZnIn_2S_4 with a 3D-hierarchical persimmon-like structure will influence the photocatalytic activity of ZnIn_2S_4 . Extending the reaction time did not reveal any significant influences on the band gap or surface area of ZnIn_2S_4 . Hence, the increase in the percentage of the {006} facet enhances hydrogen production [108]. The atomic structure of the {006} facet mainly consists of unsaturated metal cations. During the H_2 generation reaction, the exposed unsaturated Zn and In cations of ZnIn_2S_4 will attract S^{2-} and SO_3^- anions, which may help the oxidation process and speed up the consumption of photogenerated holes (Figure 8). This impedes the electron–hole recombination process, leading to improved photocatalytic activity.

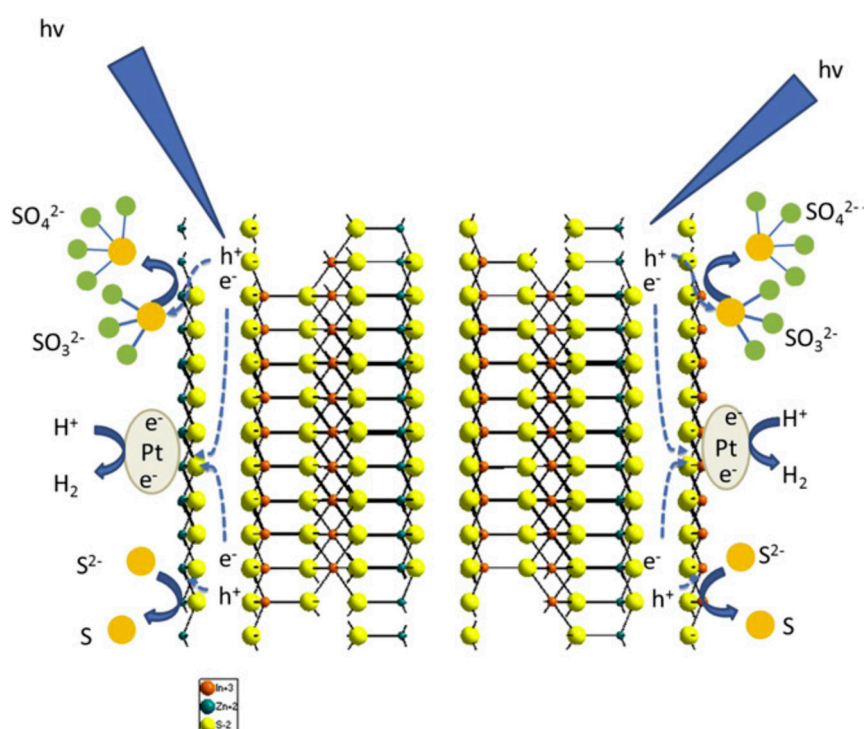


Figure 8. Schematic illustration of the hydrogen generation reaction on the {006} facets of the Pt loaded ZnIn_2S_4 photocatalysts. Figure adapted from reference [108].

3.6.2. Light Trapping (Light Harvesting)

It is reported that properly patterned surface textures can lead to dramatically enhanced light absorption by the photocatalyst because of the light trapping effect [32]. Some textured structures—including nanowire arrays [112], ordered mesoporous structures [113], micro-hole arrays [114], and hemisphere-array films [115,116]—are able to increase the light harvesting and photocatalytic performance of photocatalysts. Zhang et al. [112] reported that a 3D ZnO nanowire array–CdS sample exhibited substantial light-trapping enhancement in the visible light region. A schematic illustration of interface scattering when the light was irradiated on the surface of porous photocatalyst is provided in Figure 9 [116]. To enhance the light absorption efficiency, these surface textures allow multiple reflections and light scattering within the nanostructures. The incident light can travel through the cavities and decrease the optical loss. Efficient light trapping can be achieved by tuning the shape and roughness of the textured surface [117].

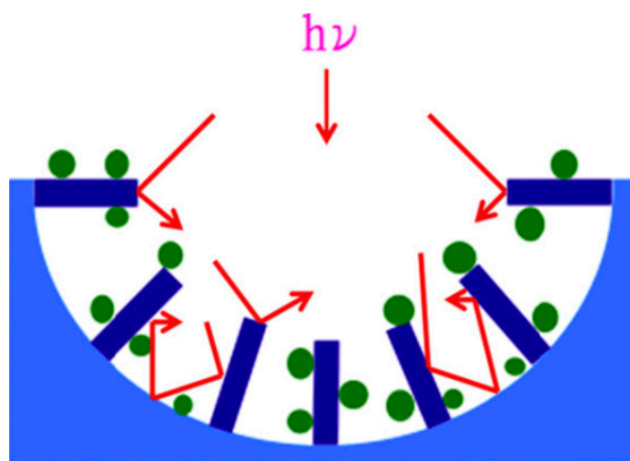


Figure 9. Schematic illustration of interface scattering due to nanograss decorated pore-array photocatalysts. Figure adapted from [116].

3.7. Fabrication Method

Photocatalysts can be prepared by numerous methods, including the coprecipitation, cation exchange, chemical bath deposition, hydrothermal, and solvothermal methods. The co-precipitation method may lead to differences between the obtained final element composition in solid solution and the stoichiometric ratio [118]. The hydrothermal method requires a great amount of time to prepare a well-crystallized solid solution [119]. In the thermolysis method, the products are treated under high temperature to achieve fast fabrication, high crystallinity, and photocatalytic performance of the solid solution [120].

Li et al. found that $Zn_{1-x}Cd_xS$ photocatalyst fabricated using the simple Zn-Cd-Tu complex thermolysis method showed better performance than did those synthesized by the coprecipitation and hydrothermal methods [118,121]. Such a thermolysis method is preferred for the following reasons: (i) the precursors can be well mixed and reacted to prepare Zn-Cd-Tu complex by the ultrasonication process; (ii) the loss of precursors can be prevented during the fabrication process; and (iii) $Zn_{1-x}Cd_xS$ with a tiny crystallite size can be prepared because thiourea releases S^{2-} ions slowly and offers some N and C atoms as the pinning points in the Zn-Cd-Tu complex [122].

Zhang et al. reported that a particular fabrication method will enable a photocatalyst to perform better in photocatalytic activity. The photocatalysts $Cd_{1-x}Zn_xS$ are prepared by three different methods: thermal sulfuration, co-precipitation without thermal treatment, and co-precipitation with thermal treatment. The photocatalyst which is synthesized by the thermal sulfuration method has better performance because the fabrication method allows uneven distribution of S^{2-} ions, thus leading to a charge gradient [123]. A similar trend is also evidenced in the work done by Park et al. on a ternary CdS/TiO₂/Pt hybrid. CdS/(Pt-sgTiO₂) has the highest hydrogen production because of the electron transfer from CdS to Pt through TiO₂ [124].

3.8. Crystal Size

Hydrogen production activity is also influenced by the crystal size of the photocatalyst. Li et al. [125] studied the photocatalytic hydrogen production performances of size-selected CdS nanoparticles decorated with co-catalyst Pt nanoparticles. When the size of CdS nanoparticles decreases from 4.6 to 2.8 nm, the H₂ generation quantum yield can increase from 11% to 17%. Such a dependence was observed because the driving force of photoinduced carrier transfer from CdS to vacant states of Pt nanoparticles is size-dependent. Baldovi et al. [126] prepared MoS₂ quantum dots by laser ablation of MoS₂ particles in suspension and investigated their photocatalytic hydrogen production performance. Two types of MoS₂ nanoparticles exhibited higher activity than that of bulk MoS₂. When the size of MoS₂ nanoparticles was decreased from 15–25 nm to 5 nm, the photocatalytic hydrogen generation

performance was almost doubled. Holmes et al. [127] and Grigioni et al. [128] reported the dependence of the photocatalytic water splitting activity on the size of CdSe nanoparticles. The photocatalytic activity increases as the size of CdSe nanoparticles decreases. Figure 10 presents the UV–vis absorption spectra and quantum yields of CdSe quantum dots photocatalysts with various size. They also reported that the light harvesting capability and the conduction band energy should compromise to achieve maximal photocatalytic H₂ generation activity. There is an optimal size of 2.8 nm to achieve maximal photocatalytic H₂ generation activity considering the compromise among light harvesting, band structure, and charge separation.

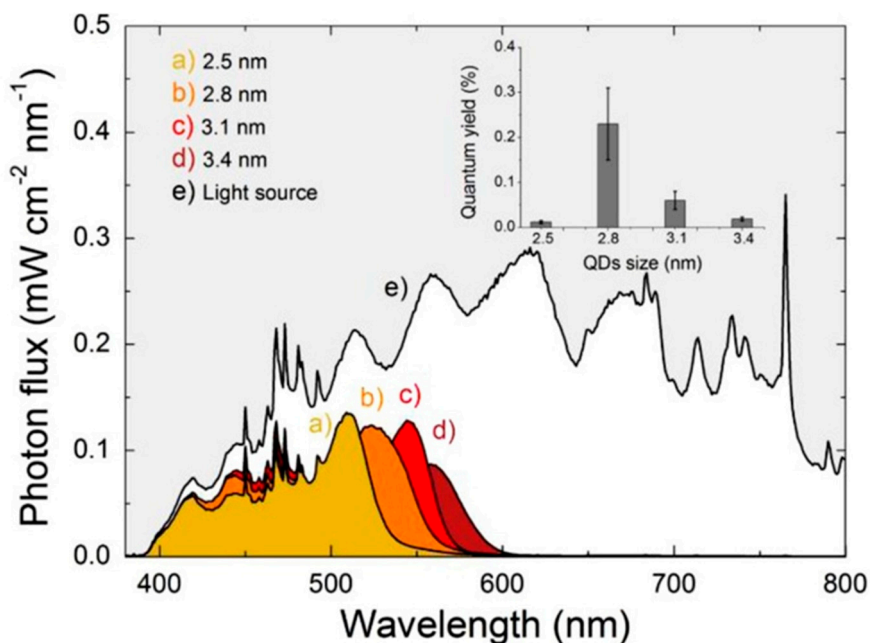


Figure 10. UV–vis absorption spectra and quantum yields of CdSe quantum dot photocatalysts with various size. Figure adapted from [128].

4. Conclusions and Perspective

In this review, we have attempted to summarize the efforts performed in the field of metal sulfide-based photocatalysts. Metal sulfide-based heterogeneous photocatalysts are promising candidates for photocatalytic hydrogen generation. Recent developments in the material design, process parameters, and performance of metal sulfide-based photocatalysts have been systematically discussed. The major problem limiting the photocatalytic H₂ generation rates of photocatalysts is the fast recombination of photoexcited electron–hole pairs. This problem can be solved by decorating with cocatalysts or incorporating noble metal nanoparticles, conductive polymers, or porous conductive substrate. The formation of heterogeneous junctions helps to promote the transport of photogenerated carriers. In-situ C K-edge NEXAFS spectra provide a new method to investigate the electronic density of the photocatalyst. It can pave the way for the rational design of photocatalysts for efficient H₂ generation. In addition, tuning the surface texture can increase the contact surface area with reactants, and the light absorption can be increased by the light trapping effect. Changing the crystal structure can also enhance the activity of a photocatalyst because of the facet effect. The fabrication of immobilized photocatalysts and magnetically separable photocatalysts makes the recycling and repeated use of photocatalysts easier to handle than photocatalyst dispersion does. The influences of doping and pH have also been discussed. The photocatalytic activity increases as the particle size of the photocatalyst decreases. This review provides a systematic overview of recent progress on the performances of various metal sulfide photocatalysts, together with some important concepts or methods to improve

and characterize their performances. Key experimental parameters and an in-situ characterization method can be applied to the research of other photocatalytic materials.

In our opinion, future research efforts should be focused on the following issues. First, we should develop in-situ spectroscopy and microscopy techniques for investigating the surface active sites, electronic states, and chemical/physical changes of the photocatalysts, together with intermediates and the mechanism of the photocatalytic reactions. Second, efforts must be focused on developing outstanding materials that can achieve both high activity and excellent reusability. Possible directions for future research are developing new heterojunction structures, increasing charge transfer, enhancing light harvesting efficiency, and achieving high activity and excellent stability of recycled photocatalysts after repeated photocatalytic H₂ production processes. Finally, to implement the use of these photocatalysts for photocatalytic hydrogen generation in industry, future works should also focus on the optimized design of reactor systems for scaled-up photocatalytic processes.

Funding: This research was supported and funded by the Ministry of Science and Technology, under the contract of MOST 105-2221-E-035-087-MY3.

Acknowledgments: The authors thank the financial support from the Ministry of Science and Technology under the contract of MOST 105-2221-E-035-087-MY3.

Conflicts of Interest: The authors declare no conflict of interest.

References

1. Norskov, J.K.; Christensen, C.H. Toward efficient hydrogen production at surfaces. *Science* **2006**, *312*, 1322–1323. [[CrossRef](#)] [[PubMed](#)]
2. Das, D.; Veziroğlu, T.N. Hydrogen production by biological processes: A survey of literature. *Int. J. Hydrogen Energy* **2001**, *26*, 13–28. [[CrossRef](#)]
3. Politano, A.; Cattelan, M.; Boukhvalov, D.W.; Campi, D.; Cupolillo, A.; Agnoli, S.; Apostol, N.G.; Lacovig, P.; Lizzit, S.; Farías, D.; et al. Unveiling the mechanisms leading to H₂ production promoted by water decomposition on epitaxial graphene at room temperature. *ACS Nano* **2016**, *10*, 4543–4549. [[CrossRef](#)]
4. Christensen, C.H.; Johannessen, T.; Sørensen, R.Z.; Nørskov, J.K. Towards an ammonia-mediated hydrogen economy? *Catal. Today* **2006**, *111*, 140–144. [[CrossRef](#)]
5. Mendoza-Damián, G.; Hernández-Gordillo, A.; Fernández-García, M.E.; Acevedo-Peña, P.; Tzompantzi-Morales, F.J.; Pérez-Hernández, R. Influence of ZnS wurtzite–sphalerite junctions on ZnO Core-ZnS Shell-1D photocatalysts for H₂ production. *Int. J. Hydrogen Energy* **2019**, *44*, 10528–10540. [[CrossRef](#)]
6. Kılıç, B.; Kılıç, Ş. Hydrogen economy model for nearly net-zero cities with exergy rationale and energy-water nexus. *Energies* **2018**, *11*, 1226. [[CrossRef](#)]
7. Weidner, J.W. Solar Energy: An Enabler of Hydrogen Economy? *Electrochem. Soc. Interface* **2018**, *27*, 45. [[CrossRef](#)]
8. Viktorsson, L.; Heinonen, J.; Skulason, J.; Unnthorsson, R. A step towards the hydrogen Economy—A life cycle cost analysis of A hydrogen refueling station. *Energies* **2017**, *10*, 763. [[CrossRef](#)]
9. Ke, X.; Dai, K.; Zhu, G.; Zhang, J.; Liang, C. In situ photochemical synthesis noble-metal-free NiS on CdS-diethylenetriamine nanosheets for boosting photocatalytic H₂ production activity. *Appl. Surf. Sci.* **2019**, *481*, 669–677. [[CrossRef](#)]
10. An, Z.; Gao, J.; Wang, L.; Zhao, X.; Yao, H.; Zhang, M.; Tian, Q.; Liu, Y. Novel microreactors of polyacrylamide (PAM) CdS microgels for admirable photocatalytic H₂ production under visible light. *Int. J. Hydrogen Energy* **2019**, *44*, 1514–1524. [[CrossRef](#)]
11. Yuan, Y.J.; Chen, D.; Yu, Z.T.; Zou, Z.G. Cadmium sulfide-based nanomaterials for photocatalytic hydrogen production. *J. Mater. Chem. A* **2018**, *6*, 11606–11630. [[CrossRef](#)]
12. Ahmad, H.; Kamarudin, S.K.; Minggu, L.J.; Kassim, M. Hydrogen from photo-catalytic water splitting process: A review. *Renew. Sustain. Energy Rev.* **2015**, *43*, 599–610. [[CrossRef](#)]
13. Majeed, I.; Nadeem, M.A.; Al-Oufi, M.; Nadeem, M.A.; Waterhouse, G.I.N.; Badshah, A.; Metson, J.B.; Idriss, H. On the role of metal particle size and surface coverage for photo-catalytic hydrogen production: A case study of the Au/CdS system. *Appl. Catal. B-Environ.* **2016**, *182*, 266–276. [[CrossRef](#)]

14. Cao, J.; Sun, J.Z.; Hong, J.; Li, H.Y.; Chen, H.Z.; Wang, M. Carbon Nanotube/CdS Core-Shell Nanowires Prepared by a Simple Room-Temperature Chemical Reduction Method. *Adv. Mater.* **2004**, *16*, 84–87. [[CrossRef](#)]
15. Chang, C.J.; Yang, T.L.; Weng, Y.C. Synthesis and characterization of Cr-doped ZnO nanorod-array photocatalysts with improved activity. *J. Solid State Chem.* **2014**, *214*, 101–107. [[CrossRef](#)]
16. Hsu, M.H.; Chang, C.J. Ag-doped ZnO nanorods coated metal wire meshes as hierarchical photocatalysts with high visible-light driven photoactivity and photostability. *J. Hazard. Mater.* **2014**, *278*, 444–453. [[CrossRef](#)]
17. Wang, X.; Liu, G.; Chen, Z.G.; Li, F.; Wang, L.; Lu, G.Q.; Cheng, H.M. Enhanced photocatalytic hydrogen evolution by prolonging the lifetime of carriers in ZnO/CdS heterostructures. *Chem. Commun.* **2009**, *23*, 3452–3454. [[CrossRef](#)]
18. Zhang, J.; Wang, Y.; Jin, J.; Zhang, J.; Lin, Z.; Huang, F.; Yu, J. Efficient visible-light photocatalytic hydrogen evolution and enhanced photostability of core-shell CdS/g-C₃N₄ nanowires. *ACS Appl. Mater. Interface* **2013**, *5*, 10317–10324. [[CrossRef](#)]
19. Yan, Z.; Sun, Z.; Liu, X.; Jia, H.; Du, P. Cadmium sulfide/graphitic carbon nitride heterostructure nanowire loading with a nickel hydroxide cocatalyst for highly efficient photocatalytic hydrogen production in water under visible light. *Nanoscale* **2016**, *8*, 4748–4756. [[CrossRef](#)]
20. Yue, X.; Yi, S.; Wang, R.; Zhang, Z.; Qiu, S. Cadmium sulfide and nickel synergetic co-catalysts supported on graphitic carbon nitride for visible-light-driven photocatalytic hydrogen evolution. *Sci. Rep.-UK* **2016**, *6*, 22268. [[CrossRef](#)]
21. Liu, M.; Li, F.; Sun, Z.; Ma, L.; Xu, L.; Wang, Y. Noble-metal-free photocatalysts MoS₂-graphene/CdS mixed nanoparticles/nanorods morphology with high visible light efficiency for H₂ evolution. *Chem. Commun.* **2014**, *50*, 11004–11007. [[CrossRef](#)] [[PubMed](#)]
22. Sun, Z.; Chen, H.; Zhang, L.; Lu, D.; Du, P. Enhanced photocatalytic H₂ production on cadmium sulfide photocatalysts using nickel nitride as a novel cocatalyst. *J. Mater. Chem. A* **2016**, *4*, 13289–13295. [[CrossRef](#)]
23. Zong, X.; Yan, H.; Wu, G.; Ma, G.; Wen, F.; Wang, L.; Li, C. Enhancement of photocatalytic H₂ evolution on CdS by loading MoS₂ as cocatalyst under visible light irradiation. *J. Am. Chem. Soc.* **2008**, *130*, 7176–7177. [[CrossRef](#)]
24. Iwashina, K.; Iwase, A.; Ng, Y.H.; Amal, R.; Kudo, A. Z-schematic water splitting into H₂ and O₂ using metal sulfide as a hydrogen-evolving photocatalyst and reduced graphene oxide as a solid-state electron mediator. *J. Am. Chem. Soc.* **2015**, *137*, 604–607. [[CrossRef](#)] [[PubMed](#)]
25. Wang, L.; Chen, H.; Xiao, L.; Huang, J. CuS/ZnS hexagonal plates with enhanced hydrogen evolution activity under visible light irradiation. *Powder Technol.* **2016**, *288*, 103–108. [[CrossRef](#)]
26. Chen, T.; Song, C.; Fan, M.; Hong, Y.; Hu, B.; Yu, L.; Shi, W. In-situ fabrication of CuS/g-C₃N₄ nanocomposites with enhanced photocatalytic H₂-production activity via photoinduced interfacial charge transfer. *Int. J. Hydrogen Energy* **2017**, *42*, 12210–12219. [[CrossRef](#)]
27. Chang, C.J.; Weng, H.T.; Chang, C.C. CuSZnS_{1-x}O_x/g-C₃N₄ heterostructured photocatalysts for efficient photocatalytic hydrogen production. *Int. J. Hydrogen Energy* **2017**, *42*, 23568–23577. [[CrossRef](#)]
28. Chang, C.J.; Wei, Y.H.; Kuo, W.S. Free-standing CuS-ZnS decorated carbon nanotube films as immobilized photocatalysts for hydrogen production. *Int. J. Hydrogen Energy* **2018**. [[CrossRef](#)]
29. Markovskaya, D.V.; Cherepanova, S.V.; Saraev, A.A.; Gerasimov, E.Y.; Kozlova, E.A. Photocatalytic hydrogen evolution from aqueous solutions of Na₂S/Na₂SO₃ under visible light irradiation on CuS/Cd_{0.3}Zn_{0.7}S and Ni_zCd_{0.3}Zn_{0.7}S_{1+z}. *Chem. Eng. J.* **2015**, *262*, 146–155. [[CrossRef](#)]
30. Chandra, M.; Bhunia, K.; Pradhan, D. Controlled Synthesis of CuS/TiO₂ Heterostructured Nanocomposites for Enhanced Photocatalytic Hydrogen Generation through Water Splitting. *Inorg. Chem.* **2018**, *57*, 4524–4533. [[CrossRef](#)]
31. Wang, Q.; An, N.; Bai, Y.; Hang, H.; Li, J.; Lu, X.; Liu, Y.; Wang, F.; Li, Z.; Lei, Z. High photocatalytic hydrogen production from methanol aqueous solution using the photocatalysts CuS/TiO₂. *Int. J. Hydrogen Energy* **2013**, *38*, 10739–10745. [[CrossRef](#)]
32. Hsu, M.H.; Chang, C.J.; Weng, H.T. Efficient H₂ production using Ag₂S-coupled ZnO@ZnS core-shell nanorods decorated metal wire mesh as an immobilized hierarchical photocatalyst. *ACS Sustain. Chem. Eng.* **2016**, *4*, 1381–1391. [[CrossRef](#)]
33. Yue, S.; Wei, B.; Guo, X.; Yang, S.; Wang, L.; He, J. Novel Ag₂S/ZnS/carbon nanofiber ternary nanocomposite for highly efficient photocatalytic hydrogen production. *Catal. Commun.* **2016**, *76*, 37–41. [[CrossRef](#)]

34. Yang, X.; Xue, H.; Xu, J.; Huang, X.; Zhang, J.; Tang, Y.B.; Ng, W.T.; Kwong, H.L.; Meng, X.M.; Lee, C.S. Synthesis of porous ZnS:Ag₂S nanosheets by ion exchange for photocatalytic H₂ generation. *ACS Appl. Mater. Interface* **2014**, *6*, 9078–9084. [[CrossRef](#)] [[PubMed](#)]
35. Xin, Z.; Li, L.; Zhang, W.; Sui, T.; Li, Y.; Zhang, X. Synthesis of ZnS@CdS–Te composites with p–n heterostructures for enhanced photocatalytic hydrogen production by microwave-assisted hydrothermal method. *Mol. Catal.* **2018**, *447*, 1–12. [[CrossRef](#)]
36. Hao, X.; Zhou, J.; Cui, Z.; Wang, Y.; Wang, Y.; Zou, Z. Zn-vacancy mediated electron–hole separation in ZnS/g-C₃N₄ heterojunction for efficient visible-light photocatalytic hydrogen production. *Appl. Catal. B-Environ.* **2018**, *229*, 41–51. [[CrossRef](#)]
37. Nawaz, M. Morphology-controlled preparation of Bi₂S₃-ZnS chloroplast-like structures, formation mechanism and photocatalytic activity for hydrogen production. *J. Photochem. Photobiol. A Chem.* **2017**, *332*, 326–330. [[CrossRef](#)]
38. Jiang, D.; Sun, Z.; Jia, H.; Lu, D.; Du, P. A cocatalyst-free CdS nanorod/ZnS nanoparticle composite for high-performance visible-light-driven hydrogen production from water. *J. Mater. Chem. A* **2016**, *4*, 675–683. [[CrossRef](#)]
39. Li, X.; Yu, J.; Wageh, S.; Al-Ghamdi, A.A.; Xie, J. Graphene in photocatalysis: A review. *Small* **2016**, *12*, 6640–6696. [[CrossRef](#)]
40. Li, Q.; Li, X.; Wageh, S.; Al-Ghamdi, A.A.; Yu, J. CdS/graphene nanocomposite photocatalysts. *Adv. Energy Mater.* **2015**, *5*, 1500010. [[CrossRef](#)]
41. Gugliuzza, A.; Politano, A.; Drioli, E. The advent of graphene and other two-dimensional materials in membrane science and technology. *Curr. Opin. Chem. Eng.* **2017**, *16*, 78–85. [[CrossRef](#)]
42. Quiroz-Cardoso, O.; Oros-Ruiz, S.; Solis-Gomez, A.; López, R.; Gómez, R. Enhanced photocatalytic hydrogen production by CdS nanofibers modified with graphene oxide and nickel nanoparticles under visible light. *Fuel* **2019**, *237*, 227–235. [[CrossRef](#)]
43. Chu, K.W.; Lee, S.L.; Chang, C.J.; Liu, L. Recent Progress of Carbon Dot Precursors and Photocatalysis Applications. *Polymers* **2019**, *11*, 689. [[CrossRef](#)] [[PubMed](#)]
44. Chang, C.J.; Wang, C.W.; Wei, Y.H.; Chen, C.Y. Enhanced Photocatalytic H₂ Production activity of Ag-doped Bi₂WO₆-graphene Based Photocatalysts. *Int. J. Hydrogen Energy* **2018**, *43*, 11345–11354. [[CrossRef](#)]
45. Azarang, M.; Sookhikian, M.; Aliahmad, M.; Dorraj, M.; Basirun, W.J.; Goh, B.T.; Alias, Y. Nitrogen-doped graphene-supported zinc sulfide nanorods as efficient Pt-free for visible-light photocatalytic hydrogen production. *Int. J. Hydrogen Energy* **2018**, *43*, 14905–14914. [[CrossRef](#)]
46. Chang, C.J.; Lin, Y.G.; Weng, H.T.; Wei, Y.H. Photocatalytic hydrogen production from glycerol solution at room temperature by ZnO-ZnS/graphene photocatalysts. *Appl. Surf. Sci.* **2018**, *451*, 198–206. [[CrossRef](#)]
47. Chang, C.J.; Lin, Y.G.; Chao, P.Y.; Chen, J.K. AgI-BiOI-graphene composite photocatalysts with enhanced interfacial charge transfer and photocatalytic H₂ production activity. *Appl. Surf. Sci.* **2019**, *469*, 703–712. [[CrossRef](#)]
48. Zhang, J.; Wang, P.; Sun, J.; Jin, Y. High-Efficiency Plasmon-Enhanced and Graphene-Supported Semiconductor/Metal Core–Satellite Hetero-Nanocrystal Photocatalysts for Visible-Light Dye Photodegradation and H₂ Production from Water. *ACS Appl. Mater. Interface* **2014**, *6*, 19905–19913. [[CrossRef](#)]
49. Chang, C.J.; Wei, Y.H.; Huang, K.P. Photocatalytic hydrogen production by flower-like graphene supported ZnS composite photocatalysts. *Int. J. Hydrogen Energy* **2017**, *42*, 23578–23586. [[CrossRef](#)]
50. Novoselov, K.S.; Geim, A.K.; Morozov, S.V.; Jiang, D.A.; Zhang, Y.; Dubonos, S.V.; Grigorieva, I.V.; Firsov, A.A. Electric field effect in atomically thin carbon films. *Science* **2004**, *306*, 666–669. [[CrossRef](#)]
51. Nethravathi, C.; Nisha, T.; Ravishankar, N.; Shivakumara, C.; Rajamathi, M. Graphene–nanocrystalline metal sulphide composites produced by a one-pot reaction starting from graphite oxide. *Carbon* **2009**, *47*, 2054–2059. [[CrossRef](#)]
52. Tsai, M.H.; Chang, C.J.; Lu, H.H.; Liao, Y.F.; Tseng, I.H. Properties of magnetron-sputtered moisture barrier layer on transparent polyimide/graphene nanocomposite film. *Thin Solid Films* **2013**, *544*, 324–330. [[CrossRef](#)]
53. Reddy, P.M.; Chang, C.J.; Lai, C.F.; Su, M.J.; Tsai, M.H. Improved organic-inorganic/graphene hybrid composite as encapsulant for white LEDs: Role of graphene, titanium (IV) isopropoxide and diphenylsilanediol. *Compos. Sci. Technol.* **2018**, *165*, 95–105. [[CrossRef](#)]

54. Mathkar, A.; Tozier, D.; Cox, P.; Ong, P.; Galande, C.; Balakrishnan, K.; Reddy, A.L.M.; Ajayan, P.M. Controlled, stepwise reduction and band gap manipulation of graphene oxide. *J. Phys. Chem. Lett.* **2012**, *3*, 986–991. [[CrossRef](#)] [[PubMed](#)]
55. Zhu, Y.; Murali, S.; Cai, W.; Li, X.; Suk, J.W.; Potts, J.R.; Ruoff, R.S. Graphene and graphene oxide: Synthesis, properties, and applications. *Adv. Mater.* **2010**, *22*, 3906–3924. [[CrossRef](#)]
56. Dreyer, D.R.; Park, S.; Bielawski, C.W.; Ruoff, R.S. The chemistry of graphene oxide. *Chem. Soc. Rev.* **2010**, *39*, 228–240. [[CrossRef](#)]
57. Yan, J.A.; Xian, L.; Chou, M.Y. Structural and electronic properties of oxidized graphene. *Phys. Rev. Lett.* **2009**, *103*, 086802. [[CrossRef](#)]
58. Zhuo, S.; Shao, M.; Lee, S.T. Upconversion and downconversion fluorescent graphene quantum dots: Ultrasonic preparation and photocatalysis. *ACS Nano* **2012**, *6*, 1059–1064. [[CrossRef](#)]
59. Yeh, T.F.; Syu, J.M.; Cheng, C.; Chang, T.H.; Teng, H. Graphite oxide as a photocatalyst for hydrogen production from water. *Adv. Funct. Mater.* **2010**, *20*, 2255–2262. [[CrossRef](#)]
60. Peng, T.; Li, K.; Zeng, P.; Zhang, Q.; Zhang, X. Enhanced photocatalytic hydrogen production over graphene oxide–cadmium sulfide nanocomposite under visible light irradiation. *J. Phys. Chem. C* **2012**, *116*, 22720–22726. [[CrossRef](#)]
61. Hou, J.; Wang, Z.; Kan, W.; Jiao, S.; Zhu, H.; Kumar, R.V. Efficient visible-light-driven photocatalytic hydrogen production using CdS@TaON core–shell composites coupled with graphene oxide nanosheets. *J. Mater. Chem.* **2012**, *22*, 7291–7299. [[CrossRef](#)]
62. Zhang, J.; Yu, J.; Jaroniec, M.; Gong, J.R. Noble metal-free reduced graphene oxide–Zn_xCd_{1–x}S nanocomposite with enhanced solar photocatalytic H₂-production performance. *Nano Lett.* **2012**, *12*, 4584–4589. [[CrossRef](#)]
63. Wang, X.; Yin, L.; Liu, G. Light irradiation-assisted synthesis of ZnO–CdS/reduced graphene oxide heterostructured sheets for efficient photocatalytic H₂ evolution. *Chem. Commun.* **2014**, *50*, 3460–3463. [[CrossRef](#)]
64. Zhang, J.; Qi, L.; Ran, J.; Yu, J.; Qiao, S.Z. Ternary NiS/Zn_xCd_{1–x}S/Reduced Graphene Oxide Nanocomposites for Enhanced Solar Photocatalytic H₂-Production Activity. *Adv. Energy Mater.* **2014**, *4*, 1301925. [[CrossRef](#)]
65. Lee, S.L.; Chang, C.J. Recent Developments about Conductive Polymer Based Composite Photocatalysts. *Polymers* **2019**, *11*, 206. [[CrossRef](#)]
66. Chang, C.J.; Chu, K.W. ZnS/polyaniline composites with improved dispersing stability and high photocatalytic hydrogen production activity. *Int. J. Hydrogen Energy* **2016**, *41*, 21764–21773. [[CrossRef](#)]
67. Wang, C.; Hu, Z.Y.; Zhao, H.; Yu, W.; Wu, S.; Liu, J.; Chen, L.; Li, Y.; Su, B.L. Probing conducting polymers@cadmium sulfide core–shell nanorods for highly improved photocatalytic hydrogen production. *J. Colloid Interface Sci.* **2018**, *521*, 1–10. [[CrossRef](#)] [[PubMed](#)]
68. Zielińska, B.; Schmidt, B.; Mijowska, E.; Kaleńczuk, R. PANI/NaTaO₃ composite photocatalyst for enhanced hydrogen generation under UV light irradiation. *Pol. J. Chem. Technol.* **2017**, *19*, 115–119. [[CrossRef](#)]
69. Sasikala, R.; Gaikwad, A.P.; Jayakumar, O.D.; Girija, K.G.; Rao, R.; Tyagi, A.K.; Bharadwaj, S.R. Nanohybrid MoS₂-PANI-CdS photocatalyst for hydrogen evolution from water. *Colloids Surf. A* **2015**, *481*, 485–492. [[CrossRef](#)]
70. Chang, C.J.; Chao, P.Y. Efficient photocatalytic hydrogen production by doped ZnS grown on Ni foam as porous immobilized photocatalysts. *Int. J. Hydrogen Energy* **2019**. [[CrossRef](#)]
71. Hsu, M.H.; Chang, C.J. S-doped ZnO nanorods on stainless-steel wire mesh as immobilized hierarchical photocatalysts for photocatalytic H₂ production. *Int. J. Hydrogen Energy* **2014**, *39*, 16524–16533. [[CrossRef](#)]
72. Chang, C.J.; Lee, Z.; Wei, M.; Chang, C.C.; Chu, K.W. Photocatalytic hydrogen production by magnetically separable Fe₃O₄@ZnS and NiCo₂O₄@ZnS core–shell nanoparticles. *Int. J. Hydrogen Energy* **2015**, *40*, 11436–11443. [[CrossRef](#)]
73. Chang, C.J.; Lee, Z.; Chu, K.W.; Wei, Y.H. CoFe₂O₄@ZnS core–shell spheres as magnetically recyclable photocatalysts for hydrogen production. *J. Taiwan Inst. Chem. Eng.* **2016**, *66*, 386–393. [[CrossRef](#)]
74. Murdoch, M.G.I.N.; Waterhouse, G.I.N.; Nadeem, M.A.; Metson, J.B.; Keane, M.A.; Howe, R.F.; Llorca, J.; Idriss, H. The effect of gold loading and particle size on photocatalytic hydrogen production from ethanol over Au/TiO₂ nanoparticles. *Nat. Chem.* **2011**, *3*, 489. [[CrossRef](#)]
75. Sun, F.; Qiao, X.; Tan, F.; Wang, W.; Qiu, X. One-step microwave synthesis of Ag/ZnO nanocomposites with enhanced photocatalytic performance. *J. Mater. Sci.* **2012**, *47*, 7262–7268. [[CrossRef](#)]
76. Sreethawong, T.; Yoshikawa, S. Comparative investigation on photocatalytic hydrogen evolution over Cu-, Pd-, and Au-loaded mesoporous TiO₂ photocatalysts. *Catal. Commun.* **2005**, *6*, 661–668. [[CrossRef](#)]

77. Zhou, H.; Pan, J.; Ding, L.; Tang, Y.; Ding, J.; Guo, Q.; Fan, T.; Zhang, D. Biomass-derived hierarchical porous CdS/M/TiO₂ (M = Au, Ag, Pt, Pd) ternary heterojunctions for photocatalytic hydrogen evolution. *Int. J. Hydrogen Energy* **2014**, *39*, 16293–16301. [[CrossRef](#)]
78. Zhang, J.; Wang, Y.; Zhang, J.; Lin, Z.; Huang, F.; Yu, J. Enhanced photocatalytic hydrogen production activities of Au-loaded ZnS flowers. *ACS Appl. Mater. Interface* **2013**, *5*, 1031–1037. [[CrossRef](#)]
79. Pany, S.; Naik, B.; Martha, S.; Parida, K. Plasmon induced nano Au particle decorated over S, N-modified TiO₂ for exceptional photocatalytic hydrogen evolution under visible light. *ACS Appl. Mater. Interface* **2014**, *6*, 839–846. [[CrossRef](#)]
80. Yu, X.; Shavel, A.; An, X.; Luo, Z.; Ibáñez, M.; Cabot, A. Cu₂ZnSnS₄-Pt and Cu₂ZnSnS₄-Au heterostructured nanoparticles for photocatalytic water splitting and pollutant degradation. *J. Am. Chem. Soc.* **2014**, *136*, 9236–9239. [[CrossRef](#)]
81. Yan, H.; Yang, J.; Ma, G.; Wu, G.; Zong, X.; Lei, Z.; Shi, J.; Li, C. Visible-light-driven hydrogen production with extremely high quantum efficiency on Pt–PdS/CdS photocatalyst. *J. Catal.* **2009**, *266*, 165–168. [[CrossRef](#)]
82. Manjunath, K.; Souza, V.S.; Nagaraju, G.; Santos, J.M.L.; Dupont, J.; Ramakrishnappa, T. Superior activity of the CuS–TiO₂/Pt hybrid nanostructure towards visible light induced hydrogen production. *New J. Chem.* **2016**, *40*, 10172–10180. [[CrossRef](#)]
83. Liu, G.; Zhao, L.; Ma, L.; Guo, L. Photocatalytic H₂ evolution under visible light irradiation on a novel Cd_xCu_yZn_{1-x-y}S catalyst. *Catal. Commun.* **2008**, *9*, 126–130. [[CrossRef](#)]
84. Kimi, M.; Yuliati, L.; Shamsuddin, M. Preparation and characterization of In and Cu co-doped ZnS photocatalysts for hydrogen production under visible light irradiation. *J. Energy Chem.* **2016**, *25*, 512–516. [[CrossRef](#)]
85. Jang, J.S.; Ji, S.M.; Bae, S.W.; Son, H.C.; Lee, J.S. Optimization of CdS/TiO₂ nano-bulk composite photocatalysts for hydrogen production from Na₂S/Na₂SO₃ aqueous electrolyte solution under visible light ($\lambda \geq 420$ nm). *J. Photochem. Photobiol. A Chem.* **2007**, *188*, 112–119. [[CrossRef](#)]
86. Wang, X.; Liu, G.; Lu, G.Q.; Cheng, H.M. Stable photocatalytic hydrogen evolution from water over ZnO–CdS core–shell nanorods. *Int. J. Hydrogen Energy* **2010**, *35*, 8199–8205. [[CrossRef](#)]
87. Chen, W.; Wang, Y.; Liu, M.; Gao, L.; Mao, L.; Fan, Z.; Shangguan, W. In situ photodeposition of cobalt on CdS nanorod for promoting photocatalytic hydrogen production under visible light irradiation. *Appl. Surf. Sci.* **2018**, *444*, 485–490. [[CrossRef](#)]
88. Zhou, H.; Liu, Y.; Zhang, L.; Li, H.; Liu, H.; Li, W. Transition metal-doped amorphous molybdenum sulfide/graphene ternary cocatalysts for excellent photocatalytic hydrogen evolution: Synergistic effect of transition metal and graphene. *J. Colloid Interface Sci.* **2019**, *533*, 287–296. [[CrossRef](#)]
89. Wang, H.; Tsai, C.; Kong, D.; Chan, K.; Abild-Pedersen, F.; Nørskov, J.K.; Cui, Y. Transition-metal doped edge sites in vertically aligned MoS₂ catalysts for enhanced hydrogen evolution. *Nano Res.* **2015**, *8*, 566–575. [[CrossRef](#)]
90. Weng, Y.C.; Chou, Y.D.; Chang, C.J.; Chan, C.C.; Chen, K.Y.; Su, Y.F. Screening of ZnS-based photocatalysts by scanning electrochemical microscopy and characterization of potential photocatalysts. *Electrochim. Acta* **2014**, *125*, 354–361. [[CrossRef](#)]
91. Chang, C.J.; Chu, K.W.; Hsu, M.H.; Chen, C.Y. Ni-doped ZnS decorated graphene composites with enhanced photocatalytic hydrogen-production performance. *Int. J. Hydrogen Energy* **2015**, *40*, 14498–14506. [[CrossRef](#)]
92. Zhang, X.; Jing, D.; Liu, M.; Guo, L. Efficient photocatalytic H₂ production under visible light irradiation over Ni doped Cd_{1-x}Zn_xS microsphere photocatalysts. *Catal. Commun.* **2008**, *9*, 1720–1724. [[CrossRef](#)]
93. Chang, C.J.; Lee, Z.; Wang, C.F. Photocatalytic hydrogen production by stainless steel@ZnS core–shell wire mesh photocatalyst from saltwater. *Int. J. Hydrogen Energy* **2014**, *39*, 20754–20763. [[CrossRef](#)]
94. Rajaambal, S.; Sivaranjani, K.; Gopinath, C.S. Recent developments in solar H₂ generation from water splitting. *J. Chem. Sci.* **2015**, *127*, 33–47. [[CrossRef](#)]
95. Asahi, R.; Morikawa, T.; Ohwaki, T.; Aoki, K.; Taga, Y. Visible-light photocatalysis in nitrogen-doped titanium oxides. *Science* **2001**, *293*, 269–271. [[CrossRef](#)]
96. Tsuji, I.; Kudo, A. H₂ evolution from aqueous sulfite solutions under visible-light irradiation over Pb and halogen-codoped ZnS photocatalysts. *J. Photochem. Photobiol. A Chem.* **2003**, *156*, 249–252. [[CrossRef](#)]
97. Hong, E.; Kim, J.H. Oxide content optimized ZnS–ZnO heterostructures via facile thermal treatment process for enhanced photocatalytic hydrogen production. *Int. J. Hydrogen Energy* **2014**, *39*, 9985–9993. [[CrossRef](#)]

98. Chang, C.J.; Huang, K.L.; Chen, J.K.; Chu, K.W.; Hsu, M.H. Improved photocatalytic hydrogen production of ZnO/ZnS based photocatalysts by Ce doping. *J. Taiwan Inst. Chem. Eng.* **2015**, *55*, 82–89. [[CrossRef](#)]
99. Li, Y.; Ma, G.; Peng, S.; Lu, G.; Li, S. Photocatalytic H₂ evolution over basic zincoxysulfide (ZnS_{1-x-0.5y}O_x(OH)_y) under visible light irradiation. *Appl. Catal. A-Gen.* **2009**, *363*, 180–187. [[CrossRef](#)]
100. Simon, T.; Bouchonville, N.; Berr, M.J.; Vaneski, A.; Adrović, A.; Volbers, D.; Wyrwich, R.; Döblinger, M.; Susha, A.S.; Rogach, A.L.; et al. Redox shuttle mechanism enhances photocatalytic H₂ generation on Ni-decorated CdS nanorods. *Nat. Mater.* **2014**, *13*, 1013. [[CrossRef](#)]
101. Zhang, Z.; Liu, K.; Feng, Z.; Bao, Y.; Dong, B. Hierarchical sheet-on-sheet ZnIn₂S₄/gC₃N₄ heterostructure with highly efficient photocatalytic H₂ production based on photoinduced interfacial charge transfer. *Sci. Rep.* **2016**, *6*, 19221. [[CrossRef](#)] [[PubMed](#)]
102. Amirav, L.; Alivisatos, A.P. Photocatalytic hydrogen production with tunable nanorod heterostructures. *J. Phys. Chem. Lett.* **2010**, *1*, 1051–1054. [[CrossRef](#)]
103. Chang, C.J.; Hsu, M.H.; Weng, Y.C.; Tsay, C.Y.; Lin, C.K. Hierarchical ZnO nanorod-array films with enhanced photocatalytic performance. *Thin Solid Films* **2013**, *528*, 167–174. [[CrossRef](#)]
104. Panmand, R.P.; Sethi, Y.A.; Deokar, R.S.; Late, D.J.; Gholap, H.M.; Baeg, J.O.; Kale, B.B. In situ fabrication of highly crystalline CdS decorated Bi₂S₃ nanowires (nano-heterostructure) for visible light photocatalyst application. *RSC Adv.* **2016**, *6*, 23508–23517. [[CrossRef](#)]
105. Chang, C.J.; Tsai, M.H.; Hsu, Y.H.; Tuan, C.S. Morphology and optoelectronic properties of ZnO rod array/conjugated polymer hybrid films. *Thin Solid Films* **2008**, *516*, 5523–5526. [[CrossRef](#)]
106. Xu, H.; Yi, J.; She, X.; Liu, Q.; Song, L.; Chen, S.; Yang, Y.; Song, Y.; Lou, J.; Li, H.; et al. 2D heterostructure comprised of metallic 1T-MoS₂/Monolayer O-g-C₃N₄ towards efficient photocatalytic hydrogen evolution. *Appl. Catal. B-Environ.* **2018**, *220*, 379–385. [[CrossRef](#)]
107. Ding, J.; Hong, B.; Luo, Z.; Sun, S.; Bao, J.; Gao, C. Mesoporous monoclinic CaIn₂S₄ with surface nanostructure: An efficient photocatalyst for hydrogen production under visible light. *J. Phys. Chem. C* **2014**, *118*, 27690–27697. [[CrossRef](#)]
108. Shen, J.; Zai, J.; Yuan, Y.; Qian, X. 3D hierarchical ZnIn₂S₄: The preparation and photocatalytic properties on water splitting. *Int. J. Hydrogen Energy* **2012**, *37*, 16986–16993. [[CrossRef](#)]
109. Li, R.; Zhang, F.; Wang, D.; Yang, J.; Li, M.; Zhu, J.; Zhou, X.; Han, H.; Li, C. Spatial separation of photogenerated electrons and holes among {010} and {110} crystal facets of BiVO₄. *Nat. Commun.* **2013**, *4*, 1432. [[CrossRef](#)]
110. Ohno, T.; Sarukawa, K.; Matsumura, M. Crystal faces of rutile and anatase TiO₂ particles and their roles in photocatalytic reactions. *New J. Chem.* **2002**, *26*, 1167–1170. [[CrossRef](#)]
111. Zhang, K.; Lin, Y.; Muhammad, Z.; Wu, C.; Yang, S.; He, Q.; Zheng, X.; Chen, S.; Ge, B.; Song, L. Active {010} facet-exposed Cu₂MoS₄ nanotube as high-efficiency photocatalyst. *Nano Res.* **2017**, *10*, 3817–3825. [[CrossRef](#)]
112. Bai, Z.; Yan, X.; Li, Y.; Kang, Z.; Cao, S.; Zhang, Y. 3D-Branched ZnO/CdS Nanowire Arrays for Solar Water Splitting and the Service Safety Research. *Adv. Energy Mater.* **2016**, *6*, 1501459. [[CrossRef](#)]
113. Li, W.; Wu, Z.; Wang, J.; Elzatahry, A.A.; Zhao, D. A perspective on mesoporous TiO₂ materials. *Chem. Mater.* **2013**, *26*, 287–298. [[CrossRef](#)]
114. Liu, H.; Zhou, H.; Ding, J.; Zhang, D.; Zhu, H.; Fan, T. Hydrogen evolution via sunlight water splitting on an artificial butterfly wing architecture. *Phys. Chem. Chem. Phys.* **2011**, *13*, 10872–10876. [[CrossRef](#)]
115. Chang, C.J.; Kuo, E.H. Light-trapping effects and dye adsorption of ZnO hemisphere-array surface containing growth-hindered nanorods. *Colloids Surf. A Physicochem. Eng. Asp.* **2010**, *363*, 22–29. [[CrossRef](#)]
116. Hung, S.T.; Chang, C.J.; Hsu, M.H. Improved photocatalytic performance of ZnO nanograss decorated pore-array films by surface texture modification and silver nanoparticle deposition. *J. Hazard. Mater.* **2011**, *198*, 307–316. [[CrossRef](#)]
117. Kluth, O.; Rech, B.; Houben, L.; Wieder, S.; Schöpe, G.; Beneking, C.; Wagner, H.; Löffel, A.; Schock, H.W. Texture etched ZnO: Al coated glass substrates for silicon based thin film solar cells. *Thin Solid Films* **1999**, *351*, 247–253. [[CrossRef](#)]
118. Xing, C.; Zhang, Y.; Yan, W.; Guo, L. Band structure-controlled solid solution of Cd_{1-x}Zn_xS photocatalyst for hydrogen production by water splitting. *Int. J. Hydrogen Energy* **2006**, *31*, 2018–2024. [[CrossRef](#)]
119. Wang, X.; Liu, G.; Chen, Z.G.; Li, F.; Lu, G.Q.M.; Cheng, H.M. Efficient and stable photocatalytic H₂ evolution from water splitting by (Cd_{0.8}Zn_{0.2})S nanorods. *Electrochem. Commun.* **2009**, *11*, 1174–1178. [[CrossRef](#)]

120. Sung, Y.M.; Lee, Y.J.; Park, K.S. Kinetic Analysis for Formation of Cd_{1-x}Zn_xSe Solid-Solution Nanocrystals. *J. Am. Chem. Soc.* **2006**, *128*, 9002–9003. [[CrossRef](#)]
121. Wang, L.; Wang, W.; Shang, M.; Yin, W.; Sun, S.; Zhang, L. Enhanced photocatalytic hydrogen evolution under visible light over Cd_{1-x}Zn_xS solid solution with cubic zinc blend phase. *Int. J. Hydrogen Energy* **2010**, *35*, 19–25. [[CrossRef](#)]
122. Li, Q.; Meng, H.; Zhou, P.; Zheng, Y.; Wang, J.; Yu, J.; Gong, J. Zn_{1-x}Cd_xS Solid Solutions with Controlled Bandgap and Enhanced Visible-Light Photocatalytic H₂-Production Activity. *ACS Catal.* **2013**, *3*, 882–889. [[CrossRef](#)]
123. Zhang, K.; Jing, D.; Xing, C.; Guo, L. Significantly improved photocatalytic hydrogen production activity over Cd_{1-x}Zn_xS photocatalysts prepared by a novel thermal sulfuration method. *Int. J. Hydrogen Energy* **2007**, *32*, 4685–4691. [[CrossRef](#)]
124. Park, H.; Choi, W.; Hoffmann, M.R. Effects of the preparation method of the ternary CdS/TiO₂/Pt hybrid photocatalysts on visible light-induced hydrogen production. *J. Mater. Chem.* **2008**, *18*, 2379–2385. [[CrossRef](#)]
125. Li, W.; O'Dowd, G.; Whittles, T.J.; Hesp, D.; Gründer, Y.; Dhanak, V.R.; Jäckel, F. Colloidal dual-band gap cell for photocatalytic hydrogen generation. *Nanoscale* **2015**, *7*, 16606–16610. [[CrossRef](#)]
126. Baldoví, H.G.; Latorre-Sánchez, M.; Esteve-Adell, I.; Khan, A.; Asiri, A.M.; Kosa, S.A.; Garcia, H. Generation of MoS₂ quantum dots by laser ablation of MoS₂ particles in suspension and their photocatalytic activity for H₂ generation. *J. Nanopart. Res.* **2016**, *18*, 240–248. [[CrossRef](#)]
127. Holmes, M.A.; Townsend, T.K.; Osterloh, F.E. Quantum confinement controlled photocatalytic water splitting by suspended CdSe nanocrystals. *Chem. Commun.* **2012**, *48*, 371–373. [[CrossRef](#)]
128. Grigioni, I.; Bernareggi, M.; Sinibaldi, G.; Dozzi, M.V.; Selli, E. Size-dependent performance of CdSe quantum dots in the photocatalytic evolution of hydrogen under visible light irradiation. *Appl. Catal. A-Gen.* **2016**, *518*, 176–180. [[CrossRef](#)]



© 2019 by the authors. Licensee MDPI, Basel, Switzerland. This article is an open access article distributed under the terms and conditions of the Creative Commons Attribution (CC BY) license (<http://creativecommons.org/licenses/by/4.0/>).